Renewable Energy 131 (2019) 1186–1207

Contents lists available at ScienceDirect

Renewable Energy

journal homepage: www.elsevier.com/locate/renene

Prediction of dynamic response of semi-submersible floating offshore wind turbine using augmented Morison's equation with frequency dependent hydrodynamic coefficients

Takeshi Ishihara [a], Shining Zhang [b, *]

[a] Department of Civil Engineering, School of Engineering, The University of Tokyo, Japan,7-3-1 Hongo, Bunkyo, 113-8656 Tokyo, Japan
[b] Climate Change & Environment Research Division, Economy & Technology Research Institute, Global Energy Interconnection Development and Cooperation Organization, 100031 Beijing, China

ARTICLE INFO

Article history:
Received 1 June 2017
Received in revised form
5 August 2018
Accepted 12 August 2018
Available online 14 August 2018

Keywords:
Floating offshore wind turbine system
Dynamic response
Morison's equation
Correction factors
Axial Froude-Krylov force
Mooring fairlead tension

ABSTRACT

A fully coupled nonlinear simulation tool using Morison's equation is developed to predict the dynamic response of floating offshore wind turbine (FOWT) system. Water tank tests are conducted to investigate hydrodynamic coefficients and the performance of the simulation tool under different sea states. Three issues are discussed in this paper. First, correction factors for the added mass and drag coefficients are proposed to account for the effects of frequency dependent hydrodynamic coefficients, and the effects of these correction factors on the global matrices are validated by the forced oscillation tests. Then, the effects of the frequency dependent hydrodynamic coefficients and the axial Froude-Krylov force on slender members are clarified by the free decay tests and water tank tests with regular and irregular waves. Finally, the dynamic behavior of mooring system on the fairlead tension is investigated by using quasi-static and dynamic models, respectively. The dynamic responses of FOWT with improved hydrodynamic models agree well with those measured in the water tank tests.

1. Introduction

Offshore wind has more energy potential compared with onshore because of much higher wind speed. It is estimated that the total offshore wind energy potential in the USA is approximately 4150 GW [1]; the theoretical offshore wind energy potential in Japan is estimated to be 1600 GW, with 80% of its wind resources located in deep water (>50 m) [2]. According to GWEC [3], global new installed offshore wind power is 4.3.GW and global cumulative value has been 18.8 GW in 2017. In deep water, floating offshore wind turbine (hereinafter referred to as "FOWT") is an innovative, prospective, and attractive design to capture the vast offshore wind energy. Owing to continuous support from government and intense R&D, several full-scale FOWTs have come to reality. The world's first full-scale 2.3 MW spar FOWT in Hywind project was installed in Norway by Statoil Hydro in 2009 [4], and the second prototype was the 2 MW semi-submersible FOWT in WindFloat project deployed in Portugal by Principle Power in 2011 [5]. In Japan, a 2 MW spar FOWT in GOTO-FOWT project was built off the coast of Kabashima in 2013 [6]. In addition, another 2 MW semi-submersible FOWT and a 7 MW V-shape semi-submersible FOWT in Fukushima FORWARD project were completed off the coast of Fukushima in 2013 and 2015 respectively [7].

An accurate evaluation of hydrodynamic force is important for the prediction of dynamic response of FOWT under different sea states. Potential flow theory and Morison's equation [8] are widely used to evaluate hydrodynamic loads. Potential flow theory accounts for the Froude-Krylov forces and diffraction effects for a large rigid body, but it cannot evaluate drag coefficients due to the viscosity of water, so the global drag matrix should be calculated from the member-level Morison drag terms as mentioned by Robertson et al. [9]. In addition, two issues remained in terms of the hydrodynamic coefficients used in Morison's equation. One is the determination of frequency dependent hydrodynamic coefficients. The other is the calculation of correction factors for the distributed hydrodynamic coefficients when the global hydrodynamic coefficients have been obtained from the water tank tests. The global matrices of hydrodynamic coefficients of the floater should be consistent with those obtained from the water tank tests. This consistence also needs to be assured in the simulations

* Corresponding author.
E-mail address: shining-zhang@geidco.org (S. Zhang).

https://doi.org/10.1016/j.renene.2018.08.042
0960-1481/

incorporated with the quadratic viscous damping, such as the distributed drag coefficients used in FAST. With a conventional Morison's equation, Sethuraman et al. [10] examined the hydrodynamic response of a floating spar wind turbine under regular and irregular waves by the industry standard time-domain modeling tool, OrcaFlex [11]. Phuc and Ishihara [12], and Waris and Ishihara [13] used an augmented Morison's equation to analyze the dynamic response of a semi-submersible FOWT and showed some differences between predicted response and those from the water tank test, which indicates Morison's equation needs to be further improved.

FAST (Fatigue, Aerodynamics, Structures, and Turbulence) developed by National Renewable Energy Laboratory [14] is one of the programs using potential theory to predict the dynamic response of FOWT, in which the floating platform is modeled with a rigid body, and concentrated mass on a single point is adopted. Nonlinear quadratic viscous drag forces are incorporated into the hydrodynamic force after FAST released its version 8. Potential flow theory-based hydrodynamic model can be used to predict the motion response of the platform to a sufficiently accurate level [15–17]. However, the rigid platform assumption will lead to a different tower natural frequency from the real one, and rigid body dynamic response makes it impossible to capture the elastic motion of the structural elements. In contrast to rigid body dynamic response analysis, elastic body dynamic response is performed by modeling the structural components with finite element method (FEM), and the distributed hydrodynamic force acting on each member is evaluated according to Morison's equation. CAsT (Computer Aided Aerodynamic and Aeroelastic Technology), developed by Phuc and Ishihara [12], is one of the simulation tools using Morison's equation and elastic body model. The commercial code Bladed [18] provides an option to use potential flow theory or Morison's equation. The study by Phuc and Ishihara [12] highlighted that the dynamic response of flexible floating platform might be underestimated by the rigid body assumption.

The mooring system is critical for station-keeping of FOWT in sea states. A comprehensive literature review in terms of dynamic modeling and quasi-static modeling of mooring system was provided in the study by Hall et al. [16,19]. The quasi-static model in the form of either force-displacement relationships or analytical solutions for catenary cables in static equilibrium is used in some simulation tools, such as FAST [14] and Bladed [18], because of its computational efficiency. Quasi-static model is suitable to predict the dynamic motion of the platform, since the dynamic force on mooring lines compared with those on the platform and wind turbine are minimal [14]. However, the effects of dynamic behavior of mooring system on the dynamic motion of the platform and mooring line fairlead tension might be significant in cases where the motion of the platform is significant. Since quasi-static model has shown its deficiency in fairlead tension prediction not only in the model test [16], but also in the field measurement [20], dynamic mooring line models including added mass, mooring line inertia, and nonlinear hydrodynamic drag force should be employed and validated.

Several studies using the dynamic model of mooring system have been performed recently [13,16,19,21,22]. The dynamic analysis for platform-mooring coupling system can be classified into de-coupling and full-coupling analysis. In the de-coupling analysis, the mooring tension is calculated according to the given instantaneous displacement of the platform, while in the full-coupling analysis, the computed fairlead tension is transferred to the force on the platform and several iterations in each time step are performed until final convergence is reached. In general, de-coupling analysis is applicable for dynamic response of FOWT with catenary mooring system, since fairlead tension in mooring line is small. However, fairlead tension in the TLP (Tension Leg Platform) is extraordinarily substantial, and therefore, a dynamic model with full-coupling analysis is definitely necessary [17]. In the study by Hall et al. [16], fairlead tension predicted by de-coupling dynamic model analysis matched well with measured fairlead tension. Since poor fairlead tension agreement was recorded when full-coupling analysis was conducted [16], the accuracy of dynamic modeling mooring system in prediction of fairlead tension using full-coupling analysis should be validated against the water tank test.

In this study, section 2 describes two scaled water tank tests and a comprehensive data set to determine frequency dependent hydrodynamic coefficients. Numerical models are described in section 3, including the equation of motion, wave theory, numerical scheme and hydrodynamic coefficients. Correction factors for hydrodynamic coefficients from a steady flow are proposed to assure consistence between global hydrodynamic coefficients and those from the water tank tests. Section 4 shows the effects of frequency dependent hydrodynamic coefficients and validates the accuracy of hydrodynamic models used in this study. Impact of dynamic behaviors of the mooring system on the dynamic response of FOWT and fairlead tensions is investigated. The accuracy of predicted dynamic response is validated by the water tank tests. Finally, conclusions of this study are summarized in section 5.

2. Water tank tests

Two water tank tests are carried out in this study. One is used to examine the hydrodynamic coefficients of FOWT and validate those used in numerical simulations. The other is employed to investigate the dynamic response of scaled FOWT under various sea states and to validate the performance of the proposed hydrodynamic models.

2.1. Forced oscillation tests

In order to identify the added mass coefficient and drag coefficient for the 1/50 scaled platform used in Fukushima FORWARD project [7], forced oscillation tests in horizontal, vertical, and rotational directions are carried out.

In this test, the model is forced to oscillate sinusoidally as shown in Eq. (1) and Eq. (2).

$$x(t) = a\sin(\omega_o t) \tag{1}$$

$$\theta(t) = \theta_a \sin(\omega_o t) \tag{2}$$

where, $x(t)$ and $\theta(t)$ are time-varying displacements in translational and rotational directions, respectively, a and θ_a are the oscillating amplitudes, ω_o is the oscillating frequency ($=2\pi/T_o$), and T_o is the oscillating period.

The time series of hydrodynamic force, $F_H(t)$, associated with the added mass coefficient and drag coefficient is obtained by subtracting the body inertia force, $F_I(t)$; hydrostatic force, $F_K(t)$; and radiation damping force, $F_r(t)$, from the measured force, $F(t)$.

$$F_H(t) = F(t) - F_I(t) - F_K(t) - F_r(t) \tag{3}$$

where,

$$F_I(t) = -M\ddot{x}(t) \tag{4}$$

$$F_K(t) = -K_R x(t) = \rho_w g A_w x(t) \tag{5}$$

$$F_r(t) = -C_r\dot{x}(t) \tag{6}$$

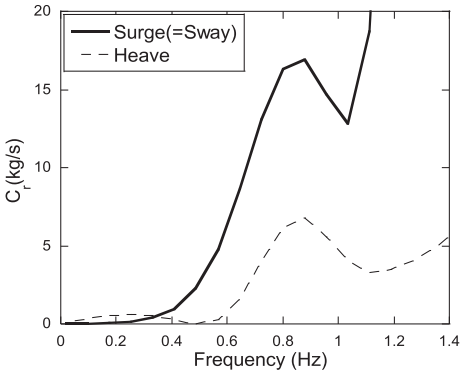

Fig. 1. Oscillating frequency-dependent radiation damping coefficients obtained from potential flow theory.

$$A_w = N_{sc}\frac{\pi D_{sc}^2}{4} + \frac{\pi D_{cc}^2}{4} + N_{brace}\frac{\pi D_{brace}^2}{4\sin(\theta_{XY})}$$

where M is the model mass including the mass of attachment used to connect the force balance and model; K_R is the hydrostatic stiffness, which is zero for the case of horizontally forced oscillation, while $K_R = \rho_w g A_w$ for the case of vertically forced oscillation; ρ_w is the water density; g is the gravitational acceleration; $\mathbf{C}_r$ is the oscillating frequency dependent on radiation damping, which is obtained from potential flow theory; $\dot{x}(t)$ and $\ddot{x}(t)$ are the velocity and acceleration of the model motion respectively, A_w is the water plane area and is calculated using the elements passing through the water surface (SC-1, SC-2, SC-3, CC, Brace-1, Brace-2, Brace-3) as shown in Fig. 5, N_{sc} and N_{brace} are the number of side columns and braces, D_{sc}, D_{cc} and D_{brace} are diameters of side column, center column and brace, θ_{XY} is the angle between the axial of elements and still water surface (XY plane).

$$A = \begin{cases} N_{Hp}D_{Hp}H_{Hp} + N_{Pntn}L_{Pntn}H_{Pntn}\sin(\theta_X); & \text{in horizontal direction} \\ N_{Hp}\dfrac{\pi D_{Hp}^2}{4}; & \text{in vertical direction} \end{cases}$$

The radiation damping coefficient, $\mathbf{C}_r$, resulting from the outgoing wave generated by the moving platform is evaluated from potential flow theory. The commonly used three-dimensional panel method or boundary element method (BEM) is performed by the computer program ANSYS AQWA [23]. Fig. 1 shows the oscillating frequency dependent radiation damping coefficients for each mode. The radiation damping coefficients in surge and heave modes are used to evaluate the radiation damping forces, $F_r(t)$, in the horizontally and vertically forced oscillation tests, respectively.

The hydrodynamic force and moment in Eq. (3) are expressed in the form of Morison's equation as:

$$F_H(t) = -C_a\rho_w\forall\,\ddot{x}(t) - 0.5C_d\rho_w A|\dot{x}(t)|\dot{x}(t) \tag{7}$$

$$M_H(t) = -C_{Ia}\rho_w\forall R^2\,\ddot{\theta}(t) - 0.5C_{Id}\rho_w AR^3|\dot{\theta}(t)|\dot{\theta}(t) \tag{8}$$

where C_a and C_{Ia} are the added mass and added inertia moment coefficients, $\forall$ is the volume of water displaced by the platform at its initial position, C_d and C_{Id} are drag coefficient in translational and rotational directions, R is the characteristic length, and A is the characteristic area.

As introduced in Ref. [24], Fourier averages of hydrodynamic coefficients are then obtained as follows:

$$C_a = \frac{1}{\pi\rho_w\forall\omega a}\int_0^{T_o} F_H(t)\sin(\omega t)dt \tag{9}$$

$$C_d = -\frac{3}{4\rho_w A\omega a^2}\int_0^{T_o} F_H(t)\cos(\omega t)dt \tag{10}$$

$$C_{Ia} = \frac{1}{\pi\rho_w\forall R^2\omega a}\int_0^{T_o} M_H(t)\sin(\omega t)dt \tag{11}$$

$$C_{Id} = -\frac{3}{4\rho_w AR^3\omega a^2}\int_0^{T_o} M_H(t)\cos(\omega t)dt \tag{12}$$

where N_{Hp} and N_{Pntn} are the number of heave plates and pontoons, D_{Hp} and H_{Hp} are the diameter and height of heave plates, L_{Pntn} and H_{Pntn} are the length and height of pontoons, θ_X is the angle between the axial of element and the global X coordinate.

Fig. 2 shows water tank tests for the forced oscillations. Parameters of the model are listed in Table 1. The hydrodynamic

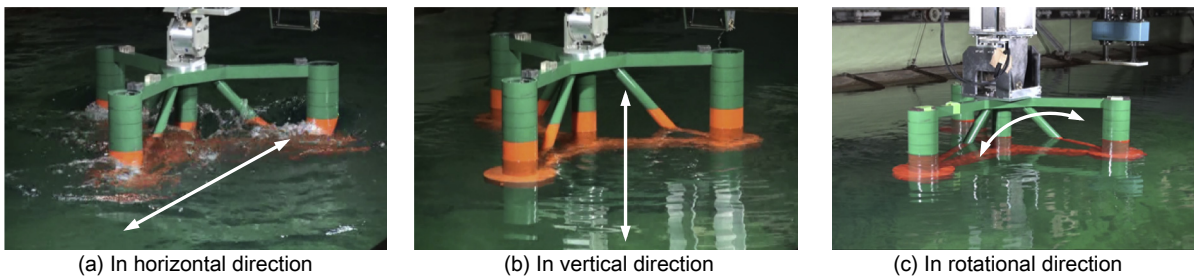

(a) In horizontal direction (b) In vertical direction (c) In rotational direction

Fig. 2. Water tank tests for the forced oscillations in (a) horizontal, (b) vertical, and (c) rotational directions.

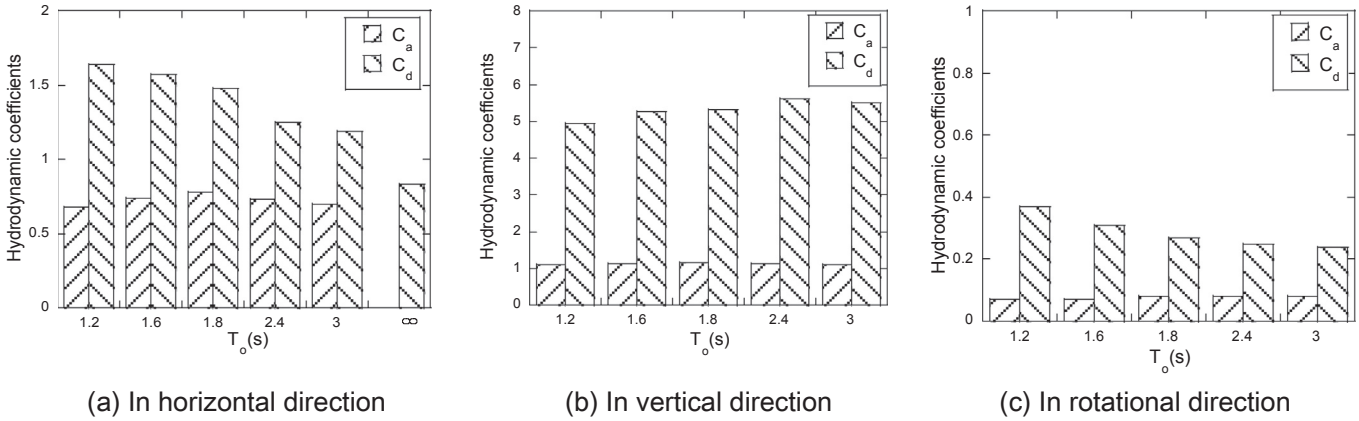

Fig. 3. Hydrodynamic coefficients in (a) horizontal direction, (b) vertical direction, and (c) rotational directions obtained from the forced oscillation tests.

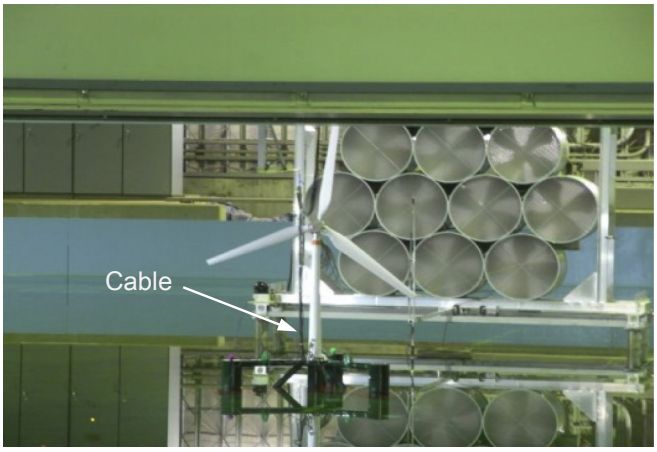

Fig. 4. The 1:50 scaled semi-submersible model used in the water tank test.

coefficient can be estimated by the measured force; 10 periods of data are used to mitigate the unstable result owing to measurement uncertainties.

The global matrices of $[C_a]$ and $[C_d]$ for one oscillating period of 3.0 are shown in Eq. (13). Diagonal terms of C_{a11} to C_{a55} and C_{d11} to C_{d55} are obtained from the water tank tests. The off-diagonal term C_{a15} and C_{d15} indicate the coupling between surge and pitch motion, while C_{a24} and C_{d24} indicate the coupling between sway and roll motion, which are also obtained from the water tank tests. The rest of off-diagonal terms in both $[C_a]$ and $[C_d]$ are almost zero owing to the symmetric geometry of floater. C_{a66} and C_{d66} are obtained by the forced oscillation in yaw direction using numerical simulation as studied in Zhang and Ishihara [25].

$$[C_a] = \begin{bmatrix} 0.70 & 0.0 & 0.0 & 0.0 & -0.08 & 0.0 \\ 0.0 & 0.70 & 0.0 & 0.08 & 0.0 & 0.0 \\ 0.0 & 0.0 & 1.11 & 0.0 & 0.0 & 0.0 \\ 0.0 & 0.08 & 0.0 & 0.08 & 0.0 & 0.0 \\ -0.08 & 0.0 & 0.0 & 0.0 & 0.08 & 0.0 \\ 0.0 & 0.0 & 0.0 & 0.0 & 0.0 & (0.11) \end{bmatrix}$$

$$[C_d] = \begin{bmatrix} 1.19 & 0.0 & 0.0 & 0.0 & -0.11 & 0.0 \\ 0.0 & 1.19 & 0.0 & 0.11 & 0.0 & 0.0 \\ 0.0 & 0.0 & 5.51 & 0.0 & 0.0 & 0.0 \\ 0.0 & 0.11 & 0.0 & 0.24 & 0.0 & 0.0 \\ -0.11 & 0.0 & 0.0 & 0.0 & 0.24 & 0.0 \\ 0.0 & 0.0 & 0.0 & 0.0 & 0.0 & (0.16) \end{bmatrix} \quad (13)$$

Fig. 3 shows the measured hydrodynamic coefficients of diagonal terms in $[C_a]$ and $[C_d]$. It is found that the added mass coefficient, C_a, shows weak oscillating period dependence in horizontal, vertical direction and rotational directions. Whereas, the drag coefficient, C_d, is a function of the oscillating period. C_d in horizontal and rotational directions decreases with increasing period, while C_d in vertical direction increases with increasing period and is expected to be larger than the value obtained in the steady flow due to the unsteady effect as shown by Zhang and Ishihara [36] and the definition of characteristic area in the vertical direction which is defined by using three heave plates and ignoring the projected area of pontoons.

In this study, one towing test is also carried out to evaluate the drag coefficient in a steady flow. The drag coefficient is obtained as follows:

$$C_d = \frac{F_d}{0.5\rho_w U^2 A} \quad (14)$$

where F_d is the measured drag force on the platform in towing direction, U refers to the towing speeds(0.2 m/s, 0.5 m/s and 1.0 m/s), and A is the characteristic area in the horizontal direction listed in Table 1. The drag coefficients obtained from three different towing speeds are then averaged as shown in Fig. 3(a), which corresponds to infinite period.

In the numerical simulation of dynamic response of the scaled FOWT, hydrodynamic coefficients at oscillating period of 3.0 s in the horizontal direction and 2.4 s in the vertical direction are used to identify the hydrodynamic coefficients used for the free decay tests. As for the prediction of the dynamic response of FOWT to regular or irregular waves, the hydrodynamic coefficients at corresponding wave period or peak period are employed.

2.2. Dynamic response tests

Dynamic responses of a 1/50 scale model for 2 MW semi-submersible FOWT [7] in various sea states are tested in National Maritime Research Institute. Dimensions of the water tank are 40 m length, 27 m width, and 2 m depth. The water depth set up in this experiment is 1.7 m. Fig. 4 shows the model used in the water tank test. Two video markers on the deck of platform and one at the top of tower are used to record the instantaneous motion of platform in six DOFs. The translational motion of platform in X, Y, and Z directions are called surge, sway, and heave motions, while the rotational motion about X, Y, and Z axes are named roll, pitch, and yaw motions respectively, as shown in Fig. 5. The origin of the coordinate system is at the free surface level. A summary of the geometry, including the diameters of each member is illustrated in Table 3. Six mooring lines,

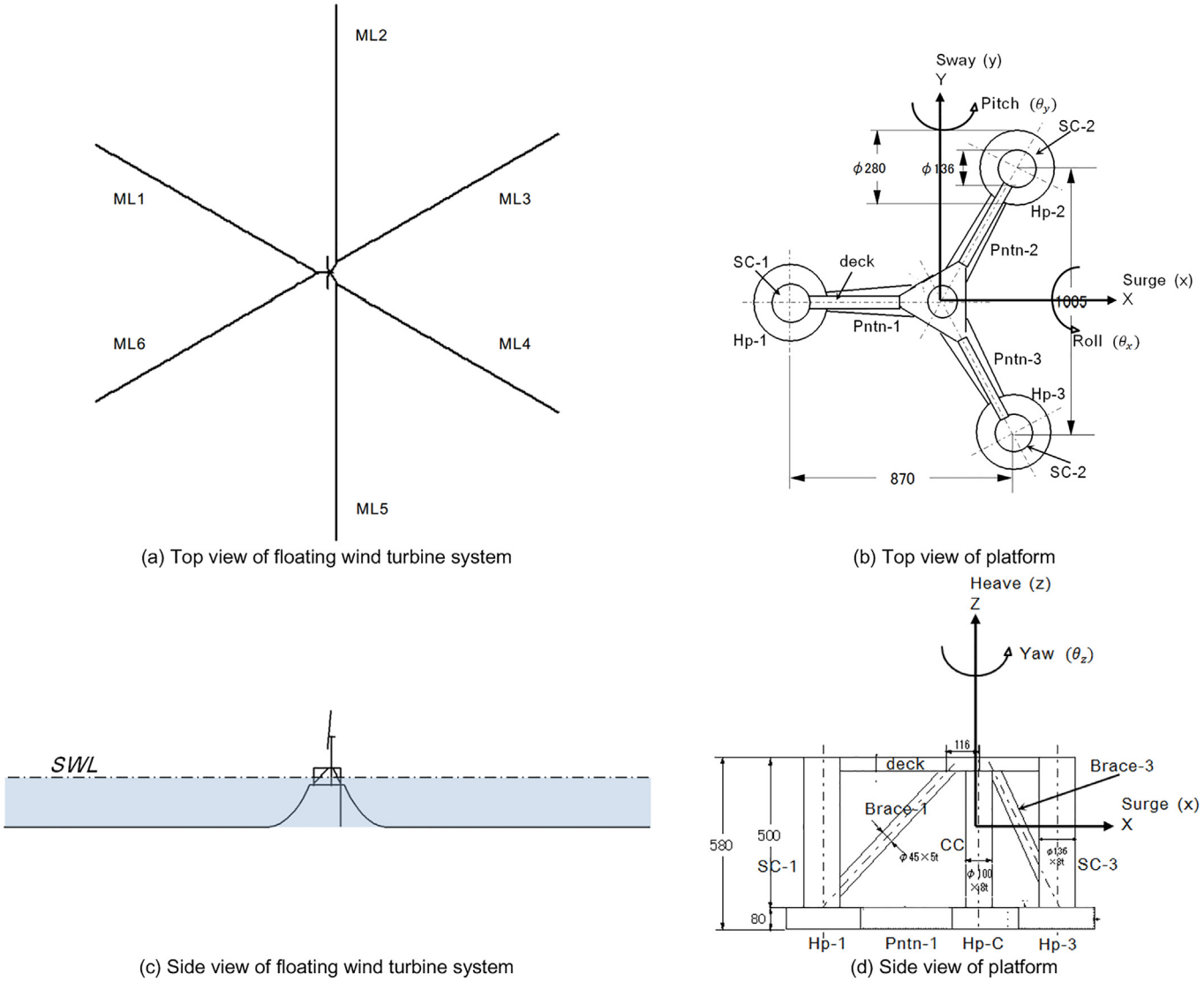

Fig. 5. Configuration of the floating wind turbine system (units: mm).

i.e., ML1 to ML6, are arranged as shown in Fig. 5(a). Each mooring line is 12.0 m length in the experimental scale and is made by connected studless chains as shown in Fig. 6. The properties of mooring chain are given in Table 2. The mass displaced by the platform is 42.2 kg including the mass of platform, wind turbine, additional mass for inclination adjustment, mass of video markers, and apparent mass of mooring line in water. Only the mass of platform and wind turbine are taken into account when measuring the center of gravity, meta-centric height, and radius of gyration.

Experimental cases are listed in Table 4. Case 1 is conducted to confirm the initial position of platform and the fairlead tension in the mooring lines. It is also used to calibrate the established numerical model. Case 2 is carried out to find the natural period of the floating system in each DOF. Response amplitude operators (RAOs) of platform in regular waves are measured in case3. Finally, an irregular sea state is carried out in case 4 to investigate responses of FOWT. Unidirectional wave generated in the experiment propagates along positive X axis in both case 3 and case 4.

3. Numerical models

A finite element model with beam, truss and spring type

Table 1
Parameters used in the forced oscillation tests.

Parameters	Symbol	Horizontal	Vertical	Rotational
Mass of platform (kg)	M	42.2	42.2	42.2
Hydrostatic stiffness (N/m,Nm/rad)	K_R	–	570.6	−14.9
Oscillating amplitude (m, rad)	a	0.1	0.04	0.052
Oscillating period (s)	T_o	1.2–3.0	1.2–3.0	1.2–3.0
Characteristic length (m)	R	–	–	1.285
Characteristic area (m^2)	A	0.3216	0.185	0.3216
Displaced volume of water (m^3)	∀	0.0422	0.0422	0.0422

Table 2
Chain properties in mooring system.

Material	Nominal Diameter D_m (mm)	Length P (mm)	Spacing W (mm)	Weight in air (N/m)	Weight in water (N/m)
Steel	3	24	5	1.432	1.246

Table 3
Hydrostatic properties of the floating offshore wind turbine model (1:50).

Elements	Dimension(m)
Total draft of the platform	0.38
Elevation of center column(tower base) and side columns(SC) above SWL	0.2
Spacing between side columns	1.005
Height of center columns (CC) and side columns	0.5
Diameter of center column	0.1
Diameter of side columns	0.136
Depth to top of heave plates(Hp) below SWL	0.3
Height of heave plates and pontoon (Pntn)	0.08
Diameter of heave plate	0.28
Width of pontoon	0.06–0.12
Length of pontoon	0.39
Diameter of brace (Brace)	0.045
Height of deck	0.045
Width of deck	0.045
Center of gravity below SWL	−0.166
meta-centric height above SWL	0.086
Radius of gyration K_{xx}	0.52
Radius of gyration K_{yy}	0.51

elements is developed to perform dynamic response analysis of full-coupled system including wind turbine, platform, and mooring system. The time domain analysis is used to efficiently capture the nonlinear characteristics of the floating system.

The equation of motion is briefly introduced first. Components of external force in terms of gravitational force, buoyancy force, hydrodynamic force, mooring tension and restoring force are described in section 3.1. Then, the wave theory used to simulate regular and irregular waves is given in section 3.2. Numerical scheme is described in section 3.3. Hydrodynamic coefficients for each element obtained from previous studies are summarized in section 3.4. Section 3.5 shows the global matrices for the hydrodynamic coefficients in the equation of integrated form. Finally, the correction factors for the added mass and drag coefficients in normal and axial direction are proposed in section 3.6.

3.1. Equation of motion in distributed form

The nonlinear equations of motion for the coupled wind turbine and support platform system is written as:

$$\mathbf{M}\{\ddot{\mathbf{x}}\} + \mathbf{C}\{\dot{\mathbf{x}}\} + \mathbf{K}\{\mathbf{x}\} = \{\mathbf{F}_G\} + \{\mathbf{F}_B\} + \{\mathbf{F}_H\} + \{\mathbf{F}_M\} + \{\mathbf{F}_R\} \quad (15)$$

where **M**, **C**, and **K** are the mass, damping and stiffness matrices of the system respectively, which are described in detail in numerical scheme in section 3.3; $\{\mathbf{x}\}$, $\{\dot{\mathbf{x}}\}$, and $\{\ddot{\mathbf{x}}\}$ are the unknown displacements in six DOFs and their time derivatives; $\{\mathbf{F}_G\}$ is the gravitational force; $\{\mathbf{F}_B\}$ refers to the buoyancy force; $\{\mathbf{F}_H\}$ means the hydrodynamic force; $\{\mathbf{F}_M\}$ stands for the force from the mooring line; and $\{\mathbf{F}_R\}$ represents the restoring force.

3.1.1. Gravitational force

Gravitational force, $\{\mathbf{F}_G\}$, includes the contribution from wind turbine, platform and mooring lines. It is directly calculated in the global coordinate system as follows:

$$\{\mathbf{F}_G\} = \{F_G^x, F_G^y; F_G^z\}^T = \{0, 0, mg\}^T \quad (16)$$

where, m is the mass of element, x, y, and z denote global coordinates.

3.1.2. Buoyancy force

Buoyancy force, $\{\mathbf{F}_B\}$, is obtained from Archimedes' principle and is nonzero only for heave DOF of the platform. The expression for the buoyancy force subjected to the elements reads:

$$\{F_B\} = \{F_B^x, F_B^y; F_B^z\}^T = \{0, 0, \rho_w g \forall\}^T \quad (17)$$

where, $\forall$ is the volume displaced by the element.

In the vertical direction, the buoyancy force balances with the gravitational force and the fairlead tension in mooring lines when the platform is at rest.

3.1.3. Hydrodynamic force

The element under water is subjected to hydrodynamic force in both normal and tangential directions. Notation of the components are expressed as follows:

$$\{\mathbf{F}_H\} = \{\mathbf{F}_H^n, \mathbf{F}_H^t\}^T = \{F_H^x, F_H^y, F_H^z\}^T \quad (18)$$

where $\{\mathbf{F}_H^n\}$ and $\{\mathbf{F}_H^t\}$ refer to the hydrodynamic force components acting on the element in the normal and tangential directions, respectively.

Morison's equation, represented by linear superposition of inertia and drag forces, is used to evaluate the hydrodynamic force in both normal and tangential directions. The inertia force is proportional to the local flow acceleration as well as the mass of water displaced by the elements. The drag force is proportional to the signed square of the instantaneous flow velocity. Illustration of force acting on a segment of slender cylinder and a heave plate is shown in Fig. 7.

(a) Chain used in the water tank test

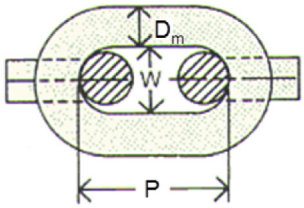

(b) Schematic chain and notations

Fig. 6. Configuration of chain used in mooring lines.

Table 4
Definition of the cases in the water tank tests.

Cases	Conditions	Description	Discussed in this paper
1	Still water	Static equilibrium test	Section 4
2	Still water	Free decay test in Surge, Sway, Heave, Roll, Pitch and Yaw directions	Section 4
3	Regular wave	H = 0.06 m; T = 1.6–3.0s	Section 4
4	Irregular wave	H_s = 0.06 m; T_p = 1.34s	Section 4

When the body moves in an oscillatory flow, hydrodynamic force acting on the element in the normal direction is expressed by the relative form of the augmented Morison's equation as:

$$\mathbf{F}_H^n = \rho_w \forall^n \dot{\mathbf{u}}^n + r_a^n C_a^n \rho_w \forall^n \dot{\mathbf{u}}^n + 0.5 r_d^n C_d^n \rho_w A^n (\mathbf{u}^n - \dot{\mathbf{x}}^n)\left|\mathbf{u}^n - \dot{\mathbf{x}}^n\right| - r_a^n C_a^n \rho_w \forall^n \ddot{\mathbf{x}}^n - \mathbf{C}_r^n \dot{\mathbf{x}}^n \quad (19)$$

where the first term at the right side of Eq. (19) accounts for the Froude-Krylov force owing to the undisturbed incident wave, and the second term represents the diffraction force resulting from pressure effects because of the presence of the structure. The third term means the drag force resulting from flow separation, and the last two terms refer to the hydrodynamic inertia force and radiation damping force caused by the motion of the structural component. Radiation damping force is neglected in the conventional Morison's equation. $\mathbf{u}^n$ and $\dot{\mathbf{u}}^n$ are the normal vectors of undisturbed velocity and acceleration of water particle on the element respectively. $\dot{\mathbf{x}}^n$ and $\ddot{\mathbf{x}}^n$ are the normal vectors of velocity and acceleration of the element motion, respectively. $\mathbf{C}_r^n$ is the frequency dependent radiation damping applied on the element located at the center of gravity; A^n is the projected area of the element in the normal direction; $\forall^n$ is the displaced volume of water of the element in the normal direction; and C_d^n is the constant drag coefficient, which is usually determined from previous studies obtained from a steady flow [26]. Since C_d^n is a function of oscillating period as shown in Fig. 3, a correction factor, r_d^n, is introduced in this study and it will be explained in section 3.6. C_a^n is a constant added mass coefficient which is commonly obtained from previous studies. The interaction between members needs to be considered; thus a correction factor, r_a^n, is also introduced in this study. Consequently, C_d^n is assumed to be the product of C_d^n obtained from steady flow and a correction factor, r_d^n obtained from the forced oscillation test. C_a^n is also multiplied by a correction factor, r_a^n, obtained from the forced oscillation test to consider the interaction between members.

As for the floating structure, hydrodynamic force along the axial (tangential) direction is significant in evaluating the dynamic response, especially for the motion in the heave direction. In order to effectively increase the hydrodynamic damping in the heave direction and reduce the heave response, appendages, such as heave plates (disks), are usually added to the keel of the vertical cylinder [27,28].

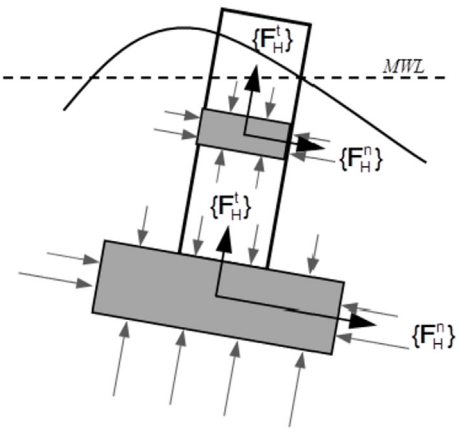

Fig. 7. Illustration of hydrodynamic forces acting on a segment of cylinder and a heave plate.

Hydrodynamic force acting on the element in the tangential direction is evaluated by the augmented Morison's equation as shown below:

$$\mathbf{F}_H^t = 0.25\pi\left[D_b^2 p_b - (D_b^2 - D_t^2) p_t\right]\mathbf{n} + r_a^t C_a^t \rho_w \forall^t \dot{\mathbf{u}}^t + 0.5 r_d^t C_d^t \rho_w A^t (\mathbf{u}^t - \dot{\mathbf{x}}^t)\left|\mathbf{u}^t - \dot{\mathbf{x}}^t\right| - r_a^t C_a^t \rho_w \forall^t \ddot{\mathbf{x}}^t - C_r^t \dot{\mathbf{x}}^t \quad (20)$$

where the first term at the right side of Eq. (20) accounts for the Froude-Krylov force, and the second term represents the diffraction force. The third term means drag force, which accounts for flow separation, and the last two terms refer to the hydrodynamic inertia force and radiation damping force; D_b and D_t are the diameters of the cross-section of element ends; P_b and P_t correspond to the dynamic pressures at the position of element ends; $\mathbf{n}$ is the unit vector along the tangential element direction; $\mathbf{u}^t$ and $\dot{\mathbf{u}}^t$ are the tangential components of undisturbed velocity and acceleration of water particle on the element respectively; $\dot{\mathbf{x}}^t$ and $\ddot{\mathbf{x}}^t$ are the tangential components of velocity and acceleration of the element motion respectively; C_r^t is the frequency-dependent radiation damping in the axial direction of element which is applied on the element located at the center of gravity; A^t is the projected area of the element in the tangential direction; $\forall^t$ is the displaced volume of water of the element in the tangential direction; C_a^t and C_d^t are the added mass and drag coefficients in the tangential direction respectively; and r_a^t and r_d^t are the correction factors of C_a^t and C_d^t respectively. C_d^t is assumed to be the product of C_d^t obtained from previous studies and correction factor, r_d^t, obtained from the forced oscillation test. Similarly, C_a^t, determined from previous studies is multiplied by a correction factor, r_a^t, obtained from the forced oscillation test to consider the interaction between members.

Wave kinematics used in Eqs. (19) and (20) and associated dynamic pressure are given in section 3.2. In Fig. 7, the equivalent wet volume is considered for those finite elements which are partially out of the water.

It should be noted that Froude-Krylov force in Eq. (20) is calculated for all elements, while the other terms in Eq. (20) are applied to the heave plate only as shown in Table 5.

Table 5
Hydrodynamic forces on elements.

Hydrodynamic force	Slender element		Heave plate	
	Normal to axial direction	Axial direction	Normal to axial direction	Axial direction
Froude-Krylov force	○	●	○	●
Diffraction force	○	N	○	●
Drag force	○	N	○	●
Added inertia force	○	N	○	●
Radiation damping force	●	N	●	●

Note: ○ indicates that the force term is included in the conventional Morison's equation; ● indicates that the new force term considered in the augmented Morison's equation; N indicates that the term is neglected.

Finally, hydrodynamic forces evaluated in Morison's equation are summarized in Table 5.

3.1.4. Mooring line force

The dynamic and quasi-static models are used to evaluate the mooring line force, $\{\mathbf{F}_M\}$, in this study. An analytical solution for the catenary mooring line force on the fairlead is widely used and known as the quasi-static model. The detailed description is given in the study by Jonkman [29]. Truss elements are used in the dynamic model to simulate the mooring line segments and to investigate the effect of dynamic behavior of mooring system. Morison's equations as shown in Eq. (19) and Eq. (20) are used to evaluate the hydrodynamic forces on mooring segments. The fairlead tension of the mooring line is calculated by the full-coupling analysis as described by Waris and Ishihara [13]. Since a portion of mooring line lies on the seabed is subjected to contact force, the contact force, $\{\mathbf{F}_C\}$, proposed by Ju et al. [30] is used and is written as follows:

$$\left\{\mathbf{F}_C\right\} = \begin{Bmatrix} \mathbf{F}_c^t \\ \mathbf{F}_c^n \end{Bmatrix} = k_p \begin{bmatrix} \mu^2 & \mu \\ \mu & 1 \end{bmatrix} \begin{Bmatrix} x^t \\ x^n \end{Bmatrix} = \{F_C^x, F_C^y, F_C^z\}^T \tag{21}$$

where μ is the coefficient of friction, x^t and x^n are the relative displacements in the tangential and normal directions, respectively, k_p is the penalty constant. The contact force at each node lying on the seabed is estimated by Eq. (21) and several iterations are carried out to satisfy the convergence criteria.

3.1.5. Restoring force

A non-hydrostatic model proposed by Waris and Ishihara [13] is employed in the simulation. The hydrostatic loads resulting from the hydrostatic pressure are dependent on the elevation of incident wave and motion of the floater itself. The restoring force, $\{\mathbf{F}_R\}$, in Eq. (15) reads:

$$\left\{\mathbf{F}_R\right\} = \mathbf{K}_R(\{\mathbf{x}\} - \{\boldsymbol{\eta}\})^T = \{F_R^x, F_R^y, F_R^z\}^T \tag{22}$$

$$\mathbf{K}_R = \begin{bmatrix} 0 & 0 & 0 \\ 0 & 0 & 0 \\ 0 & 0 & -\rho_w g A_w \end{bmatrix} \tag{23}$$

where $\mathbf{K}_R$ is the linear hydrostatic-restoring matrix from the effects of water-plane area, and $\{\boldsymbol{\eta}\}$ is the wave elevation vector, which is nonzero only in the vertical DOF. Since FEM is utilized, the contribution on rotational restoring stiffness has been considered automatically. The restoring stiffness in the horizontal direction is mainly realized by the mooring system.

3.2. Wave theory

The FOWT is located in deep water; therefore, linear wave theory is used in regular wave to provide water particle velocity and acceleration for Morison's equation. Wheeler stretching is employed to account for the kinematics of water particle above the mean water surface.

The instantaneous wave elevation, η, in the linear wave is expressed as follows:

$$\eta = \frac{H}{2}\cos(kx\text{-}\omega t) \tag{24}$$

where H is the wave height, k refers to the wave number, $\omega(=2\pi/T)$ represents the wave frequency, and T means the wave period.

Wave kinematics and associated dynamic pressure for the linear wave are obtained as below:

$$u_x = \frac{\pi H}{T}\frac{\cosh(kz+kd)}{\sinh(kd)}\cos(kx\text{-}\omega t) \tag{25}$$

$$u_z = \frac{\pi H}{T}\frac{\sinh(kz+kd)}{\sinh(kd)}\sin(kx\text{-}\omega t) \tag{26}$$

$$\dot{u}_x = \frac{\omega^2 H}{2}\frac{\cosh(kz+kd)}{\sinh(kd)}\sin(kx\text{-}\omega t) \tag{27}$$

$$\dot{u}_z = -\frac{\omega^2 H}{2}\frac{\sinh(kz+kd)}{\sinh(kd)}\cos(kx\text{-}\omega t) \tag{28}$$

$$p = \frac{\rho g H}{2}\frac{\cosh k(z+d)}{\cosh kd}\cos(kx\text{-}\omega t) \tag{29}$$

where u_x and u_z are the velocity components of water particle in x and z directions, $\dot{u}_x$ and $\dot{u}_z$ are the accelerations of water particle in x and z directions, d is the water depth.

As for the irregular wave, JONSWAP wave spectrum is used in both numerical simulation and water tank test. The spectrum is given as follows:

$$S(f) = \alpha_* H_S^2 T_P^{-4} f^{-5} \exp\left\{-1.25(T_P f)^{-4}\right\} \gamma^{\exp\left\{-\frac{(T_P f-1)^2}{2\sigma^2}\right\}} \tag{30}$$

$$\alpha_* = \frac{0.0624}{0.230 + 0.0336\gamma\text{-}0.185/(1.9+\gamma)} \tag{31}$$

where f is the wave frequency (Hz), H_s is the significant wave height, T_P is the peak wave period, γ is the peak factor, σ is the shape factor (σ=0.07 for $f \le (1/T_P)$ and $\sigma = 0.09$ for $f > (1/T_P)$).

The frequency spectrum is discretized with the number of frequencies N, and the instantaneous wave elevation, η, is represented as a finite sum of sinusoidal components [24] as follows:

$$\eta = \sum_{n=1}^{N} A_n \cos(k_n x\text{-}\omega_n t + \varepsilon_n) \tag{32}$$

where A_n, k_n, ω_n, and ε_n are the discretized wave amplitude, wave number, wave frequency and random phase respectively.

Similarly, wave kinematics and associated dynamic pressure at location (x, z) for the irregular wave are given as below:

Table 6
Description of the numerical scheme used in this study.

Term	Description
Dynamic analysis	Direct Numerical Integration (Newmark-β)
Formulation	Total Lagrangian formulation
Convergence	Newton-Raphson Method

$$u_x = \sum_{n=1}^{N} A_n \omega_n \frac{\cosh(k_n z + k_n d)}{\sinh(k_n d)} \cos(k_n x - \omega_n t + \varepsilon_n) \tag{33}$$

$$u_z = \sum_{n=1}^{N} A_n \omega_n \frac{\sinh(k_n z + k_n d)}{\sinh(k_n d)} \sin(k_n x - \omega_n t + \varepsilon_n) \tag{34}$$

$$\dot{u}_x = \sum_{n=1}^{N} A_n \omega_n^2 \frac{\cosh(k_n z + k_n d)}{\sinh(k_n d)} \sin(k_n x - \omega_n t + \varepsilon_n) \tag{35}$$

$$\dot{u}_z = -\sum_{n=1}^{N} A_n \omega_n^2 \frac{\sinh(k_n z + k_n d)}{\sinh(k_n d)} \cos(k_n x - \omega_n t + \varepsilon_n) \tag{36}$$

$$p = \sum_{n=1}^{N} A_n \omega_n^2 \frac{\cosh(k_n z + k_n d)}{\cosh k_n d} \cos(k_n x - \omega_n t + \varepsilon_n) \tag{37}$$

Wheeler stretching [31] is used to stretched the kinematics calculated at the mean water surface to the true surface by modifying the original vertical coordinate z as follows:

$$z' = \left(\frac{z - \eta}{d + \eta}\right) d \tag{38}$$

where z' is the scaled vertical coordinate and d is the water depth.

The velocity and acceleration of water particle in x and z directions are transformed to the normal and tangential directions of the element for usage in Eq. (19) and Eq. (20). The effective element length below the instantaneous wave elevation is used to evaluate the hydrodynamic loads acting on the element.

3.3. Numerical scheme and finite element model

The origin in the coordinate system is at free surface level as shown in Fig. 5. The equation of motion in numerical solutions is rewritten as follows:

$$(\mathbf{M} + \mathbf{M}_a)\{\ddot{x}\} + (\mathbf{C} + \mathbf{C}_r)\{\dot{x}\} + \mathbf{K}\{x\} = \{\mathbf{F}\} \tag{39}$$

where $\{\mathbf{F}\}$ is the external force, $\mathbf{M}_a = r_a C_a \rho_w \forall$ is the added mass from radiation force in Eq. (19) and Eq. (20), $\mathbf{C}$ is the structural damping matrix and is estimated using the Rayleigh damping model as follows:

$$\mathbf{C} = \boldsymbol{\alpha}(\mathbf{M} + \mathbf{M}_a) + \boldsymbol{\beta}\mathbf{K} \tag{40}$$

where $\mathbf{M}$ is the mass matrix, $\mathbf{M}_a$ is the added mass matrix, $\mathbf{K}$ is the stiffness matrix of the element, which depends on the element type (i.e., beam, truss, or spring element) [32,33]. The off-diagonal terms in the mass matrix for each finite element are assumed to be negligible. The mass matrix of element, i, in the numerical model is given as follows:

$$\mathbf{M_i}+\mathbf{M_{ai}} = \begin{bmatrix} m_i + m_{ai} & 0 & 0 & 0 & 0 & 0 \\ 0 & m_i + m_{ai} & 0 & 0 & 0 & 0 \\ 0 & 0 & m_i + m_{ai} & 0 & 0 & 0 \\ 0 & 0 & 0 & 0 & 0 & 0 \\ 0 & 0 & 0 & 0 & 0 & 0 \\ 0 & 0 & 0 & 0 & 0 & 0 \end{bmatrix} \tag{41}$$

$$\alpha = 2\omega_1\omega_2\left(\frac{\omega_1\zeta_2 - \omega_2\zeta_1}{\omega_1^2 - \omega_2^2}\right), \beta = 2\left(\frac{\omega_1\zeta_1 - \omega_2\zeta_2}{\omega_1^2 - \omega_2^2}\right) \tag{42}$$

where ω_1, ω_2 and ζ_1, ζ_2 are the natural frequencies and damping ratios for the heave and pitch modes; $\zeta_1 = \zeta_2 = 0.005$ are used as shown in the reference [13].

The numerical scheme is summarized in Table 6. Newmark-β method is used to solve the nonlinear equation of dynamic motion in time domain. Unconditional stable condition with $\gamma' = 1/2$ and $\beta = 1/4$ is used in the Newmark-β method. Total Lagrangian formulation is employed and the coordinate system is earth-fixed in this study. Newton-Raphson method is utilized to reach the convergent solution.

3.4. Hydrodynamic coefficients

In order to evaluate the hydrodynamic loads on the platform by Morison's equation, hydrodynamic coefficients, namely drag and added mass coefficients need to be determined first. In this study, hydrodynamic coefficients are determined from previous studies first, and correction factors for hydrodynamic coefficients are identified according to the measured coefficients obtained from the forced oscillation tests.

The drag and added mass coefficients for each component of the platform determined from previous studies are listed in Table 7. In the normal direction, ${}_iC_d^n$ is the drag coefficient for infinite long cylinders in a steady flow. An equivalent drag coefficient, C_d^n, for the whole platform in the normal direction is evaluated as follows:

$$C_d^n = \frac{\sum({}_iC_d^n A_i^n \sin^3(\theta_i))}{A^n} \tag{43}$$

where i represents each element of the platform; A_i^n and A^n refer to the characteristic areas of each element and the whole platform, respectively; and θ_i is the angle between the axial and global X directions of the element.

3.5. Equation of motion in integrated form

The distributed equation of motion as shown in Eq. (39) is integrated, and the integrated form reads

$$\sum(M + M_a)\{\ddot{x}\} + \sum(C + C_r)\{\dot{x}\} + \sum K\{x\} = \sum\{F\} \tag{44}$$

where, $\mathbf{M}_a = C_a \rho_w \forall$.

The non-zero components in the global matrices of $[C_a]$ and $[C_d]$ shown in Eq. (44) are as below.

$$[C_a] = \begin{bmatrix} C_{a11} & 0.0 & 0.0 & 0.0 & C_{a15} & 0.0 \\ 0.0 & C_{a22} & 0.0 & C_{a24} & 0.0 & 0.0 \\ 0.0 & 0.0 & C_{a33} & 0.0 & 0.0 & 0.0 \\ 0.0 & C_{a42} & 0.0 & C_{a44} & 0.0 & 0.0 \\ C_{a51} & 0.0 & 0.0 & 0.0 & C_{a55} & 0.0 \\ 0.0 & 0.0 & 0.0 & 0.0 & 0.0 & C_{a66} \end{bmatrix}$$

$$[C_d] = \begin{bmatrix} C_{d11} & 0.0 & 0.0 & 0.0 & C_{d15} & 0.0 \\ 0.0 & C_{d22} & 0.0 & C_{d24} & 0.0 & 0.0 \\ 0.0 & 0.0 & C_{d33} & 0.0 & 0.0 & 0.0 \\ 0.0 & C_{d42} & 0.0 & C_{d44} & 0.0 & 0.0 \\ C_{d51} & 0.0 & 0.0 & 0.0 & C_{d55} & 0.0 \\ 0.0 & 0.0 & 0.0 & 0.0 & 0.0 & C_{d66} \end{bmatrix} \quad (45)$$

The evaluation of non-zero components are obtained as:

$$C_{a11} = \frac{1}{\rho_w \forall} \sum_{i=1}^{N_W} \left[{}_iC_a^n \rho \forall_i^n \sin^2\theta_i + {}_iC_a^t \rho \forall_i^t \cos^2\theta_i \right]; C_{a22} = C_{a11};\ C_{a33} = \frac{1}{\rho_w \forall} \sum_{i=1}^{N_W} \left[{}_iC_a^t \rho \forall_i^t \cos^2\theta_k + {}_iC_a^n \rho \forall_i^n \sin^2\theta_k \right];$$

$$C_{a44} = C_{a55};\ C_{a55} = \frac{1}{\rho_w \forall R^2} \sum_{i=1}^{N_W} \left[{}_iC_a^t \rho \forall_i^t \cos^2\theta_k x_i^2 + {}_iC_a^n \rho \forall_i^n \sin^2\theta_k x_i^2 + {}_iC_a^n \rho \forall_i^n \sin^2\theta_i (z_i - z_G)^2 + {}_iC_a^t \rho \forall_i^t \cos^2\theta_i (z_i - z_G)^2 \right];$$

$$C_{a66} = \frac{1}{\rho_w \forall R^2} \sum_{i=1}^{N_W} {}_iC_a^n \rho \forall_i^n \left[x_i^2 + y_i^2 \right];\ C_{a15} = \frac{1}{\rho_w \forall R} \sum_{i=1}^{N_W} \left[{}_iC_a^n \rho \forall_i^n \sin^2\theta_i (z_i - z_G) + {}_iC_a^t \rho \forall_i^t \cos^2\theta_i (z_i - z_G) \right];$$

$$C_{a51} = C_{a15};\ C_{a24} = -C_{a15};\ C_{a42} = C_{a24}. \quad (46)$$

where N_W is the number of element in water, θ_j is the angle between the axial and global Y directions, $\forall_i^n$ and $\forall_i^t$ represent the projected displaced volume of element i in the surge and heave directions, (x_i, y_i, z_i) is the coordinate of the element i, and z_G is the z-coordinate of the whole floater.

$$[C_d] = \begin{bmatrix} 1.11 & 0.0 & 0.0 & 0.0 & -0.01 & 0.0 \\ 0.0 & 1.11 & 0.0 & 0.01 & 0.0 & 0.0 \\ 0.0 & 0.0 & 4.06 & 0.0 & 0.0 & 0.0 \\ 0.0 & 0.01 & 0.0 & 0.06 & 0.0 & 0.0 \\ -0.01 & 0.0 & 0.0 & 0.0 & 0.06 & 0.0 \\ 0.0 & 0.0 & 0.0 & 0.0 & 0.0 & 0.07 \end{bmatrix} \quad (48)$$

$$C_{d11} = \frac{1}{A_x} \sum_{i=1}^{N_W} \left[{}_iC_d^n A_i^n \sin^3\theta_i + {}_iC_d^t A_i^t \cos^3\theta_i \right];\ C_{d22} = C_{d11};\ C_{d33} = \frac{1}{A_z} \sum_{i=1}^{N_W} \left[{}_iC_d^t A_i^t \cos^3\theta_k + {}_iC_d^n A_i^n \sin^3\theta_k \right];$$

$$C_{d44} = C_{d55};\ C_{d55} = \frac{1}{A_x R^3} \sum_{i=1}^{N_W} \left[{}_iC_d^t A_i^t \cos^3\theta_k |x_i|^3 + {}_iC_d^n A_i^n \sin^3\theta_k |x_i|^3 + {}_iC_d^n A_i^n \sin^3\theta_i |z_i - z_G|^3 + {}_iC_d^t A_i^t \cos^3\theta_i |z_i - z_G|^3 \right];$$

$$C_{d66} = \frac{1}{A_x R^3} \sum_{i=1}^{N_w} {}_iC_d^n A_i^n \left[\left(x_i^2 + y_i^2 \right)^{3/2} \right];\ C_{d15} = -\frac{1}{A_x R^2} \sum_{i=1}^{N_W} \left[{}_iC_d^n A_i^n \sin^3\theta_i (z_i - z_G)^2 + {}_iC_d^t A_i^t \cos^3\theta_i (z_i - z_G)^2 \right];$$

$$C_{d51} = C_{d15};\ C_{d24} = -C_{d15};\ C_{d42} = C_{d24}. \quad (47)$$

where A_x and A_z are the characteristic area of the floater in the surge and heave directions, A_i^n and A_i^t represent the area of element i in the normal and tangential directions.

According to the distributed hydrodynamic coefficients given in Table 7, the global matrices of added mass and viscous damping with respect to the center of gravity is evaluated as follows:

$$[C_a] = \begin{bmatrix} 0.67 & 0.0 & 0.0 & 0.0 & -0.03 & 0.0 \\ 0.0 & 0.67 & 0.0 & 0.03 & 0.0 & 0.0 \\ 0.0 & 0.0 & 1.05 & 0.0 & 0.0 & 0.0 \\ 0.0 & 0.03 & 0.0 & 0.09 & 0.0 & 0.0 \\ -0.03 & 0.0 & 0.0 & 0.0 & 0.09 & 0.0 \\ 0.0 & 0.0 & 0.0 & 0.0 & 0.0 & 0.11 \end{bmatrix}$$

3.6. Correction factors for hydrodynamic coefficients

When the global matrices of $[C_a]$ and $[C_d]$ based on database are different from the measured ones from the water tank tests, the

Table 7
Hydrodynamic parameters for each component of the platform.

Elements	${}_iC_d^n$	${}_iC_a^n$	${}_iC_d^t$	${}_iC_a^t$
Side column SC-1	1.07 [34]	1.0 [35]	0	0
Side column SC-2	1.07 [34]	1.0 [35]	0	0
Side column SC-3	1.07 [34]	1.0 [35]	0	0
Center column *Cc*	1.07 [34]	1.0 [35]	0	0
Heave plate Hp-1	1.07 [34]	0.5 [25]	2.49 [36]	2.14 [36]
Heave plate Hp-2	1.07 [34]	0.5 [25]	2.49 [36]	2.14 [36]
Heave plate Hp-3	1.07 [34]	0.5 [25]	2.49 [36]	2.14 [36]
Center heave plate Hp-C	1.07 [34]	0.5 [25]	2.49 [36]	2.14 [36]
Pontoon Pntn-1	1.98 [37]	0.725 [35]	0	0
Pontoon Pntn-2	1.98 [37]	0.725 [35]	0	0
Pontoon Pntn-3	1.98 [37]	0.725 [35]	0	0
Brace-1	1.20 [34]	1.0 [35]	0	0
Brace-2	1.20 [34]	1.0 [35]	0	0
Brace-3	1.20 [34]	1.0 [35]	0	0
Mooring line	1.20 [38]	1.0 [38]	0	0

hydrodynamic coefficients need to be corrected. As observed in Fig. 3(a), the drag coefficient in an oscillating flow is a function of oscillating period, which means that the frequency dependent characteristics should be considered to accurately predict the dynamic response of the model in a free decay test as well as in regular and irregular waves. In this study, correction factors are proposed. Even though $[C_a]$ and $[C_d]$ are 6×6 matrix, some off-diagonal terms are zero owing to the symmetric geometry of the floater. The correction factors in the surge, sway and heave directions are obtained as shown in Eq. (49). The added inertia moment can be modified by adding one additional value on a specified node.

$$r_{a,ii}=\frac{C_{a,ii}^{I}}{C_{a,ii}^{D}};\quad r_{d,ii}=\frac{C_{d,ii}^{I}}{C_{d,ii}^{D}}\quad i=1,2,3 \tag{49}$$

where $C_{a,ii}^{I}$ and $C_{d,ii}^{I}$ are the integrated added mass and drag coefficients, $C_{a,ii}^{D}$ and $C_{d,ii}^{D}$ are the equivalent added mass and drag coefficients evaluated according to the distributed hydrodynamic coefficients.

The correction factor for the drag coefficient in the normal direction is identified as:

$$r_d^n=\frac{C_d^nA^n}{\sum\left({}_iC_d^nA_i^n\sin^3(\theta_i)\right)} \tag{50}$$

where C_d^n is the measured drag coefficient from the forced oscillation test in the horizontal direction as shown in Fig. 3(a), A^n is the characteristic area of the model in the horizontal direction as listed in Table 1, θ_i is the angle between the axial and global X directions of the element.

The correction factor for the drag coefficient of heave plate in its tangential direction is obtained as:

$$r_d^t=\frac{C_d^tA^t-\sum\left({}_iC_d^nr_d^nA_i^n\right)-\sum\left({}_jC_d^nr_d^nA_j^n\sin^3(\theta_k)\right)}{\sum\left({}_kC_d^tA_k^t\right)} \tag{51}$$

where C_d^t is the measured drag coefficient from the forced oscillation test in the vertical direction as shown in Fig. 3(b), A^t is the characteristic area of the model in the vertical direction as listed in Table 1, ${}_iC_d^n$, ${}_jC_d^n$, and ${}_kC_d^n$ are the drag coefficients of pontoons, braces and heave plates respectively, as listed in Table 7, A_i^n, A_j^n and A_k^n refer to the corresponding characteristic areas, r_d^n is the correction factor obtained by Eq. (50), θ_k is the angle between the axial and global Z directions of the braces.

The correction factor for the added mass coefficient is also calculated by comparing it with the measured added mass coefficient from the forced oscillation test. The correction factor for the added mass coefficient in the normal direction is evaluated as:

$$r_a^n=\frac{C_a^n\forall^n}{\sum\left({}_iC_a^n\forall_i^n\sin^2(\theta_i)\right)} \tag{52}$$

where C_a^n is the measured added mass coefficient in the horizontal direction as shown in Fig. 3(a), ${}_iC_a^n$ is the added mass coefficient listed in Table 7, $\forall_i^n$ and $\forall^n$ refer to the displaced volumes of water by each element and the whole platform in the normal direction, respectively, θ_i is the angle between the axial and global X directions of the element.

The correction factor for the added mass coefficient of heave plate in its tangential direction is identified as:

$$r_a^t=\frac{C_a^t\forall^t-\sum\left({}_iC_a^nr_a^n\forall_i^n\right)-\sum\left({}_jC_a^nr_a^n\forall_j^n\sin^2(\theta_k)\right)}{\sum\left({}_kC_a^t\forall_k^t\right)} \tag{53}$$

where C_a^t is the measured added mass coefficient in the vertical direction as shown in Fig. 3(b), ${}_iC_a^n$, ${}_jC_a^n$ and ${}_kC_a^n$ are the added mass coefficients of pontoons, braces and heave plates in the normal direction respectively, listed in Table 7, $\forall_i^n$ and $\forall_j^n$ refer to the corresponding displaced volumes of the element in the normal direction, $\forall_k^t$ is the displaced volume of the element in the tangential direction; r_a^n is the correction factor obtained by Eq. (52), θ_k is the angle between the axial and global Z directions of the braces.

4. Numerical results and discussion

The influence of hydrodynamic coefficients on the dynamic response of FOWT is investigated and clarified by the free decay test. Then, the significance of axial Froude-Krylov force on the dynamic response of platform is discussed according to the results in regular waves and an irregular wave. Finally, the dynamic effect of mooring system on tension prediction is investigated by examining the fairlead tension obtained by quasi-static and dynamic models.

4.1. Determination of correction factors for hydrodynamic coefficients

The platform, tower and rotor are modeled with 73, 11, and 33 beam elements respectively, to represent the floating system in the established FEM. Each rectangular pontoon shown in Fig. 5 is modeled with four varying cross-section cylindrical elements in the numerical model, and the hydrodynamic coefficient for each cylindrical element is identical in the normal direction. Each mooring line is modeled with 50 truss elements to simulate the mooring system with the dynamic model. The studless chains are modeled by cylindrical elements with a diameter of $2D_m$ (6 mm). Dimensions of other components are summarized in Table 3. By ensuring the volume displaced by the pontoon remained unchanged, each varying cross-section rectangular pontoon is modeled by four varying cross-section cylindrical elements.

The resulting $[C_a]$ and $[C_d]$ after the modification for translational DOF (Surge, Sway, and heave) are given as follows:

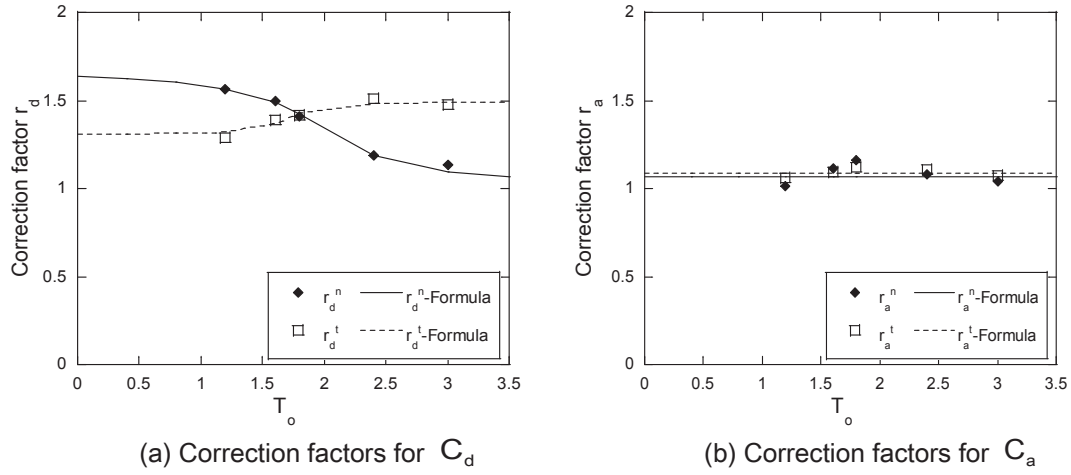

Fig. 8. Measured and predicted frequency dependent correction factors for C_d and C_a.

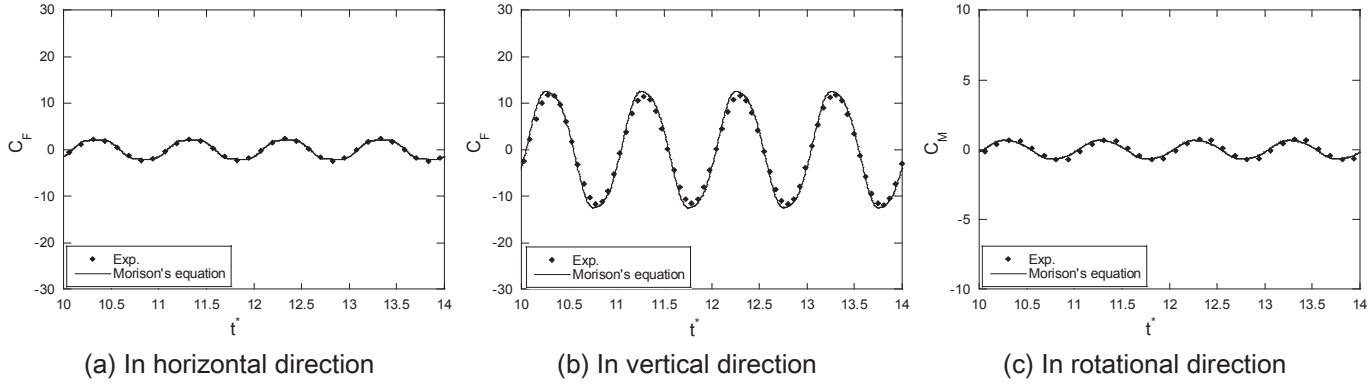

Fig. 9. Measured and predicted time history of force coefficient by Morison's equation in the forced oscillation.

Table 8
Measured and predicted amplitude of hydrodynamic force coefficient.

Direction	Measured	Predicted	Error (%)
Horizontal	2.42	2.35	−2.9%
Vertical	12.10	12.88	6.4%
Rotational	0.74	0.68	−8.1%

$$[C_a] = \begin{bmatrix} 0.70 & 0.0 & 0.0 & 0.0 & -0.03 & 0.0 \\ 0.0 & 0.70 & 0.0 & 0.03 & 0.0 & 0.0 \\ 0.0 & 0.0 & 1.11 & 0.0 & 0.0 & 0.0 \\ 0.0 & 0.03 & 0.0 & 0.09 & 0.0 & 0.0 \\ -0.03 & 0.0 & 0.0 & 0.0 & 0.09 & 0.0 \\ 0.0 & 0.0 & 0.0 & 0.0 & 0.0 & 0.11 \end{bmatrix}$$

$$[C_d] = \begin{bmatrix} 1.19 & 0.0 & 0.0 & 0.0 & -0.01 & 0.0 \\ 0.0 & 1.19 & 0.0 & 0.01 & 0.0 & 0.0 \\ 0.0 & 0.0 & 5.51 & 0.0 & 0.0 & 0.0 \\ 0.0 & 0.01 & 0.0 & 0.09 & 0.0 & 0.0 \\ -0.01 & 0.0 & 0.0 & 0.0 & 0.09 & 0.0 \\ 0.0 & 0.0 & 0.0 & 0.0 & 0.0 & 0.07 \end{bmatrix} \quad (54)$$

As can be seen from $[C_a]$, the difference in the translational DOFs between Eq. (13) and Eq. (54) are small, and are improved as well after the correction comparing Eq. (48). As for $[C_d]$, the accuracy in the surge and heave directions are also improved after the correction comparing Eq. (48). The difference for the off-diagonal term has little influence on the dynamic response of the floater motion.

Formulas of correction factors are proposed to account for frequency dependent phenomena as.

$$\begin{aligned} r_a^n &= 1.07 \times r_a^n(f); \quad r_a^n(f) = 1 \\ r_a^t &= 1.09 \times r_a^t(f); \quad r_a^t(f) = 1 \end{aligned} \quad (55)$$

$$\begin{aligned} r_d^n &= 1.34 \times r_d^n(f); \quad r_d^n(f) = \left(1 - \frac{0.52}{\pi}\tan^{-1}(2(T_o - 2.0))\right) \\ r_d^t &= 1.40 \times r_d^t(f); \quad r_d^t(f) = \left(1 + \frac{0.14}{\pi}\tan^{-1}(5(T_o - 1.7))\right) \end{aligned} \quad (56)$$

The comparison between experimentally determined and formulas predicted correction factors are shown in Fig. 8. The correction factors for C_d show significant frequency dependent, while the correction factors for C_a are almost frequency independent. Although the hydrodynamic coefficients are functions of both Reynolds number and KC number [36,39,40], the proposed correction factors for hydrodynamic coefficients in this study are focused on one specific frequency parameter-beta defined by Re/KC [24].

As for the prediction of the response to regular or irregular waves, the hydrodynamic coefficients corresponding to regular wave periods or peak periods as shown in Fig. 3 are employed to determine the correction factors.

Time history of hydrodynamic force in non-dimensional form as

a force coefficient is expressed as follows:

$$C_F(t^*) = \frac{F_H(t^*)}{0.5\rho_w A(\omega a)^2}; \quad t^* = \frac{t}{T_o} \tag{57}$$

where, $C_F(t^*)$ is the non-dimensional force coefficient, t^* is the non-dimensional time, and T_o is the oscillating period.

Fig. 9 shows the measured and predicted time series of the hydrodynamic force coefficient in forced oscillations with a period of 1.6 s listed in Table 1. Even only the hydrodynamic coefficient in the horizontal and vertical directions are directly corrected according to the water tank test, good agreement is obtained in the rotational direction as well.

The predicted amplitude of the force coefficient by Morison's equation and measured force coefficient are listed in Table 8 for quantitative comparison. The differences between the measured and predicted force coefficient amplitude in the horizontal, vertical and rotational directions are −2.9%, 6.4% and −8.1%, respectively.

The mooring system is modeled by either quasi-static or dynamic modeling in this study. Morison's equation is used to evaluate the hydrodynamic force on the mooring system in the dynamic model. Since the hydrodynamic force on the mooring system is ignored in the quasi-static model, the equivalent force is considered on the platform when using the quasi-static model in this study.

4.2. Effect of frequency dependent hydrodynamic coefficients

The effect of time step on the accuracy of simulation is discussed first. The predicted time series of non-dimensional surge motion in one sample of irregular wave with four different time step ranges from 0.005s to 0.05s are compared. Non-dimensional surge motion is defined as follows:

Table 10
Linear radiation damping coefficient at natural period obtained from potential theory.

DOF	Surge (kg/s)	Sway (kg/s)	Heave (kg/s)	Roll (kg·m²/s)	Pitch (kg·m²/s)	Yaw (kg·m²/s)
C_r	0.01	0.01	0.26	0.0	0.0	0.0

$$x^*(t^*) = \frac{x(t^*)}{H_s/2}; \quad t^* = \frac{t}{T_p} \tag{58}$$

where, x^* corresponds to the non-dimensional surge motion, t^* is the non-dimensional time, and T_P is the wave peak period of incident irregular wave.

Normalized maximum displacements are expressed as:

$$A_x^* = \frac{A_{x\text{-max}}}{H_s/2}; \quad A_z^* = \frac{A_{z\text{-max}}}{H_s/2}; \quad A_{\theta_y}^* = \frac{A_{\theta_y\text{-max}}}{H_s/2} \tag{59}$$

where $A_{x\text{-max}}$, $A_{z\text{-max}}$, and $A_{\theta_y\text{-max}}$ correspond to the maximum of motion in the surge, heave, and pitch directions, respectively.

Time history of normalized surge motion is shown in Fig. 10(a), and it can be observed that larger time step (0.02s) significantly underestimates the surge motion during non-dimensional time from 44 to 48. The simulation is independent of time step when it is less than 0.01 s. Fig. 10(b) illustrates the normalized maximum displacement in the surge, heave and pitch motions within 10-mins simulated data. It is found that the maximum of the pitch motions is underestimated when using a larger time step. The time step dt = 0.01s is finally used in this study to take into consideration of the accuracy and computational efficiency.

The static equilibrium test in still water is simulated to test the balance of floating system. Table 9 gives the initial displacement of platform and initial tension obtained from the experiment and

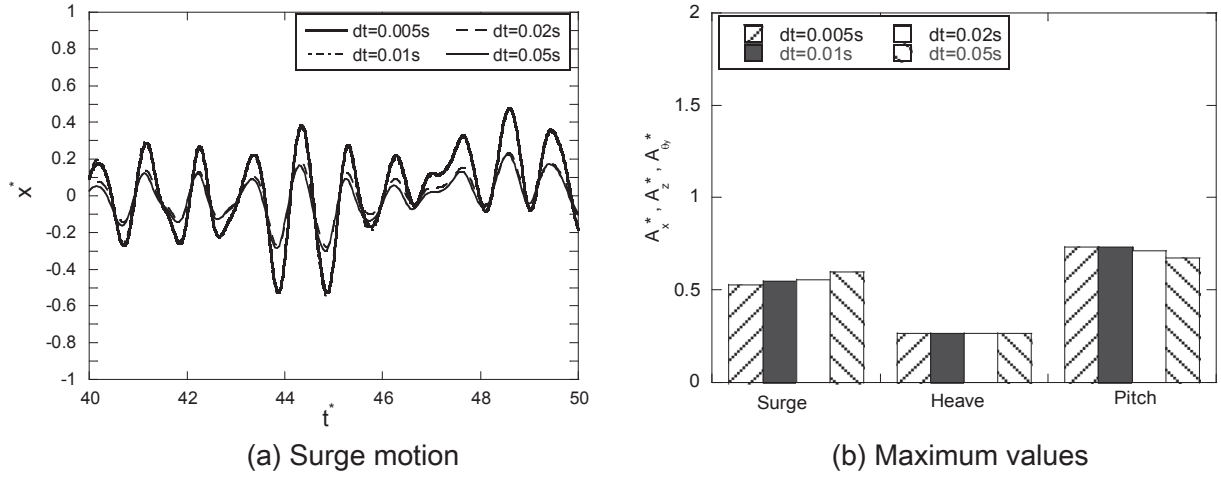

Fig. 10. Time history of non-dimensional surge motion and its maximum values in an irregular wave for four different time steps.

Table 9
Measured and predicted initial displacements of the floating system and fairlead tensions in the mooring lines.

DOF	Surge x (m)	Sway y (m)	Heave z (m)	Roll θ_x(deg.)	Pitch θ_y (deg.)	Yaw θ_z(deg.)	ML1 T1(N)	ML2 T2(N)	ML3 T3(N)
Exp.	0.051	−0.028	−0.006	0.627	−0.168	−1.582	3.12	2.78	2.58
Cal.(W/O adjustment)	0.002	0	−0.001	0	−0.555	0	2.72	2.75	2.70
Cal.(With adjustment)	0.051	0	−0.001	0	−0.233	0	3.00	2.76	2.47

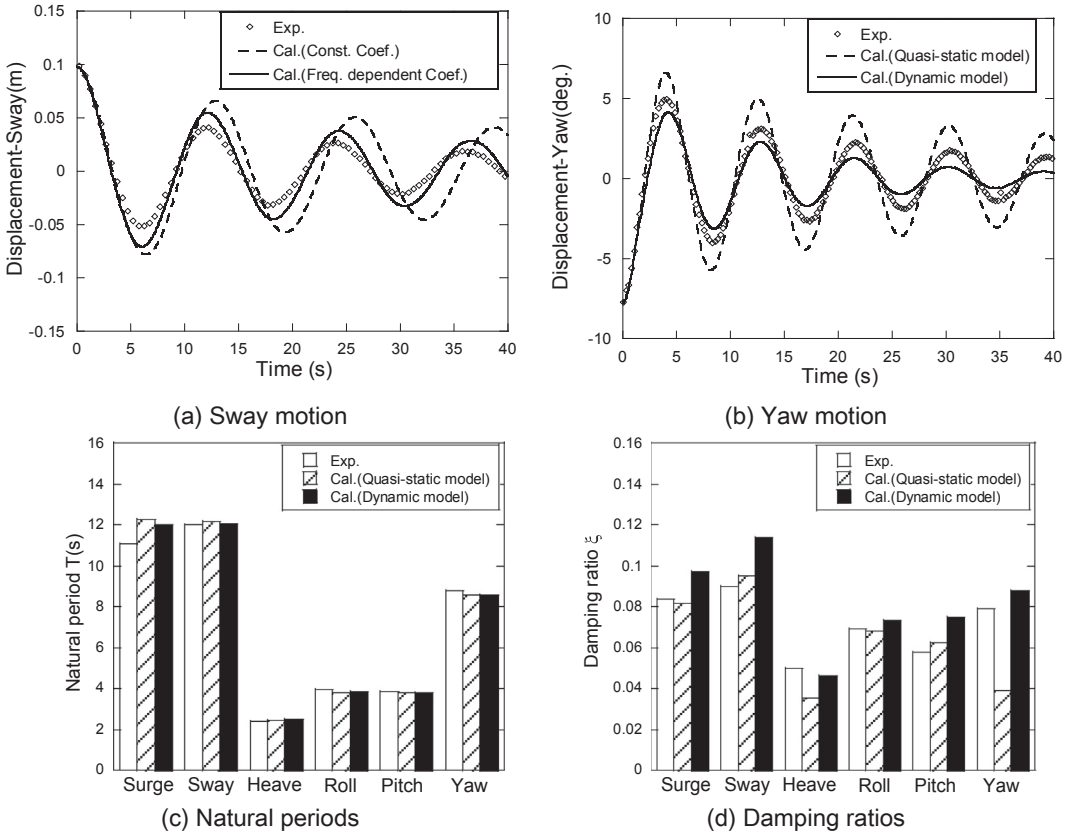

Fig. 11. Comparison of measured and predicted time series of (a) sway motion, (b) yaw motion, (c) natural periods and (b) damping ratios of the FOWT obtained from the free decay tests.

numerical simulation. In the experiment, there are some unbalanced initial displacements in the surge direction which is due to the attached cable used for transferring data at the tower base (see Fig. 4). The initially positive surge motion gives rise to the fairlead tension in mooring line ML3 smaller than those in the other two mooring lines. In order to explain the effect of the attached cable, an additional force is identified as 0.98N by matching the initial displacement in the surge direction, and is applied on the tower base. The initial values with this adjustment are also shown in Table 9. As expected, the predicted fairlead tensions match well with those in the experiment. The predicted initial sway, roll and yaw motion are zero because of the symmetric feature of the floating system. The difference between predicted and measured heave motion is negligible. Negative pitch motion is mainly caused by the weight of three blades and is improved if the effect of the attached cable is taken into account. The imperfection of experimental setup brings about non-zero initial roll and yaw displacements. The inclination in the roll direction can yield some sway displacements. Favorable agreement between predicted and measured initial conditions indicates that the established floating system model is reasonable for the following dynamic response analysis.

The accuracy of hydrodynamic coefficients shown in Table 7 without any correction is investigated by the free decay test. In addition, the simulation with consideration of corrected hydrodynamic coefficients as shown in Fig. 8 is also investigated.

The linear radiation damping coefficients corresponding to the natural period shown in Table 10 are used in the simulations when

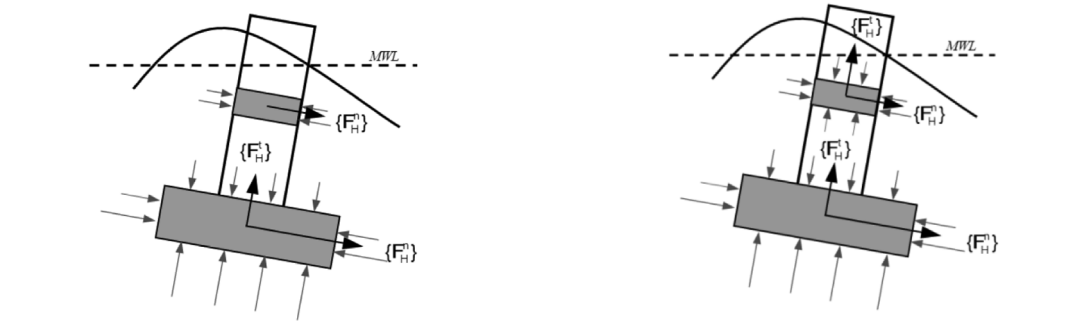

(a) Without axial F-K force acting on slender members (b) With axial F-K force acting on slender members

Fig. 12. Hydrodynamic force conditions in two sets of simulations.

evaluating the hydrodynamic force on the platform by Eq. (19). Fig. 11(a) and (b) show the measured and predicted time series of sway and yaw motions in the free decay test. “Const. Coef” and “Freq. dependent Coef.” refer to the situations where the hydrodynamic coefficients obtained from towing test are directly used and corrected by the correction factors as shown in Fig. 8, respectively.

It is found that both the amplitude of sway motion and natural period in the sway mode are overestimated when the hydrodynamic coefficients determined from the steady flow are not corrected, while both the amplitude and natural period are improved when the hydrodynamic coefficients are corrected according to the

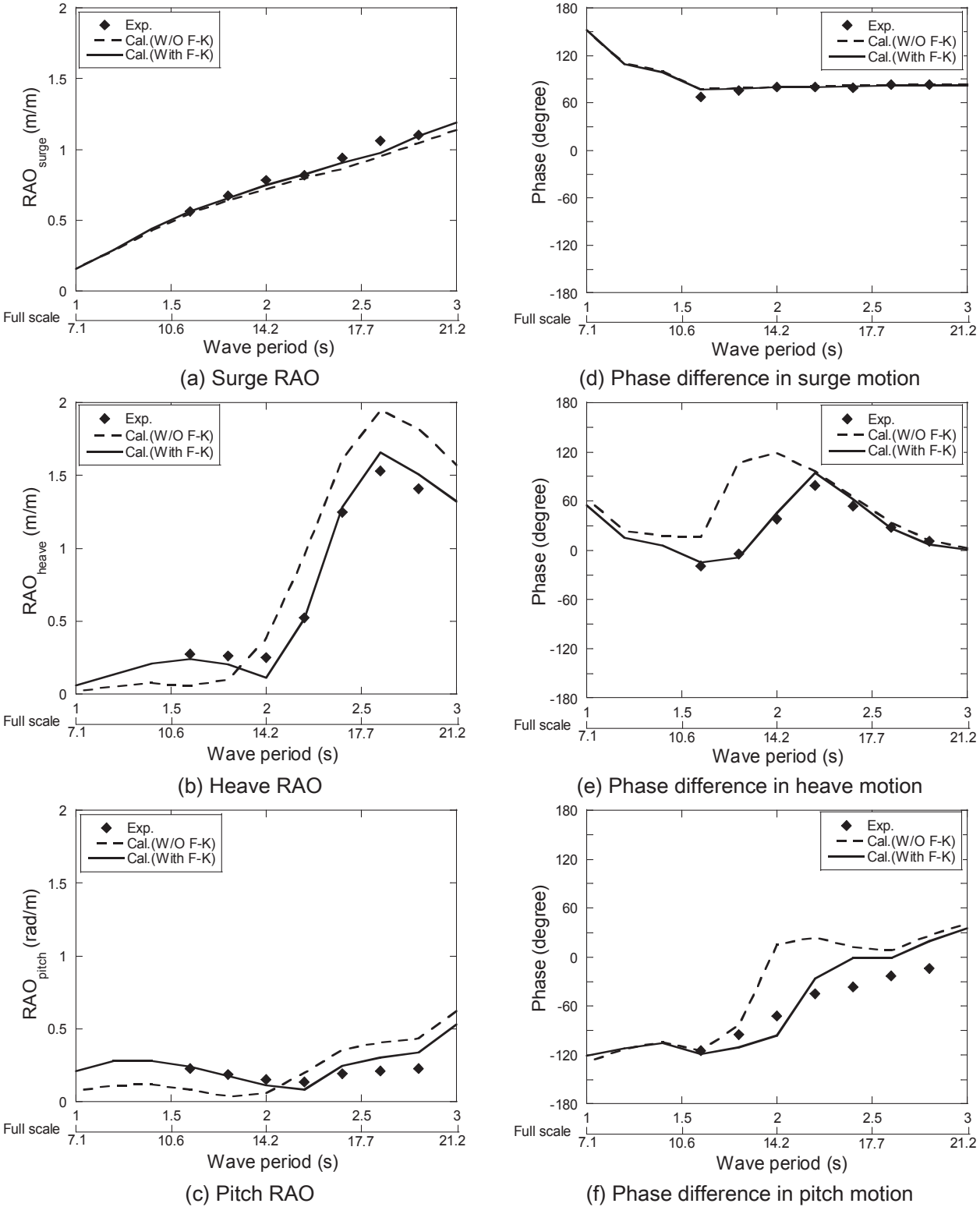

Fig. 13. Measured and predicted dynamic motion RAO and phase differences between the motions of platform and incident wave in regular waves (case 3).

results obtained from the forced oscillation test. This indicates that the effect of frequency dependent added mass and drag coefficients should be considered. As can be concluded from Fig. 11(b), the yaw motion predicted by the quasi-static model is overestimated, which is due to the neglect of hydrodynamic damping on mooring segments. In contrast to the quasi-static model, the dynamic model increases the damping since Morison's equation is used to account for the viscous drag damping.

Natural periods and damping ratios of floating system obtained from the free decay tests are shown in Fig. 11(c) and (d). The predicted natural periods in six DOFs match well with those obtained from the water tank test. The predicted natural periods of surge and sway (roll and pitch) mode are the same because of the symmetric floating system, while there is some difference in the measurement owing to the limitation of the experiment. The predicted natural period difference between quasi-static and dynamic models is negligible because the added mass provided by the mooring system is sufficiently small compared with the mass of the total floating system. Whereas, the dynamic model increases the damping especially in the yaw mode as shown in Fig. 11(d).

4.3. Effect of axial Froude-Krylov forces

The effect of axial Froude-Krylov (hereinafter referred to as "F-K") forces on slender cylinders is clarified by the simulations in regular and irregular waves (case 3 and case 4 as shown in Table 4), which is neglected in the previous study [41]. Fig. 12 illustrates two different situations in terms of distinct hydrodynamic force conditions. The case shown in Fig. 12 (a) neglects F-K force on slender cylinders, while F-K force expressed in Eq. (20) is included in the simulation as shown in Fig. 12(b). Dynamic motions of the platform are investigated, and forces under these two conditions are compared to clarify the effect of F-K force in the axial direction.

Response amplitude operator (RAO) is employed to compare the dynamic responses obtained from water tank tests and numerical simulations in regular waves. Fast Fourier Transform is applied to the time series to extract the amplitude of response corresponding to the wave frequency component. The motion RAO in the regular waves is expressed as:

$$\mathrm{RAO}_{\mathrm{surge}} = \frac{A_x}{H/2};\ \mathrm{RAO}_{\mathrm{heave}} = \frac{A_z}{H/2};\ \mathrm{RAO}_{\mathrm{pitch}} = \frac{A_{\theta_y}}{H/2} \tag{60}$$

where A_x, A_z, and A_{θ_y} refer to the amplitudes of responses in the surge, heave, and pitch directions respectively, and H refers to the incident regular wave height.

The normalized time history of wave elevation and motions of the platform are expressed as:

$$\eta^*(t^*) = \frac{\eta(t^*)}{H/2};\ t^* = \frac{t}{T} \tag{61}$$

$$x^*(t^*) = \frac{x(t^*)}{H/2};\ z^*(t^*) = \frac{z(t^*)}{H/2};\quad \theta_y^*(t^*) = \frac{\theta_y(t^*)}{H/2} \tag{62}$$

where η^* refers to the normalized wave elevation; x^*, z^*, and θ_y^* correspond to the normalized responses in the surge, heave, and pitch directions, respectively; t^* is the non-dimensional time; and T is the wave period of incident regular wave.

Fig. 13 shows the measured and predicted dynamic RAOs and phase difference between the motion of platform and the incident wave. "W/O F-K" and "With F-K" indicate that axial Froude-Krylov forces on slender members are neglected and considered,

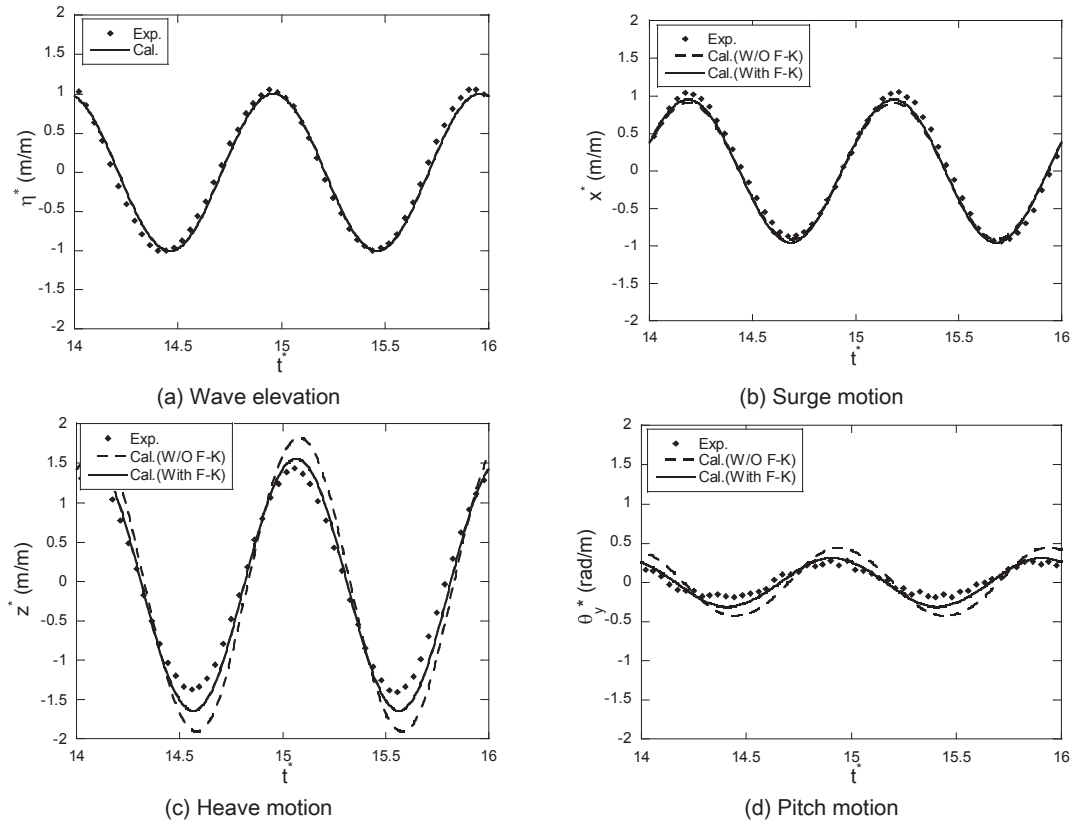

Fig. 14. Measured and predicted time series of normalized (a) wave elevation, (b) surge motion, (c) heave motion and (d) pitch motion in a regular wave with wave period of 2.6s.

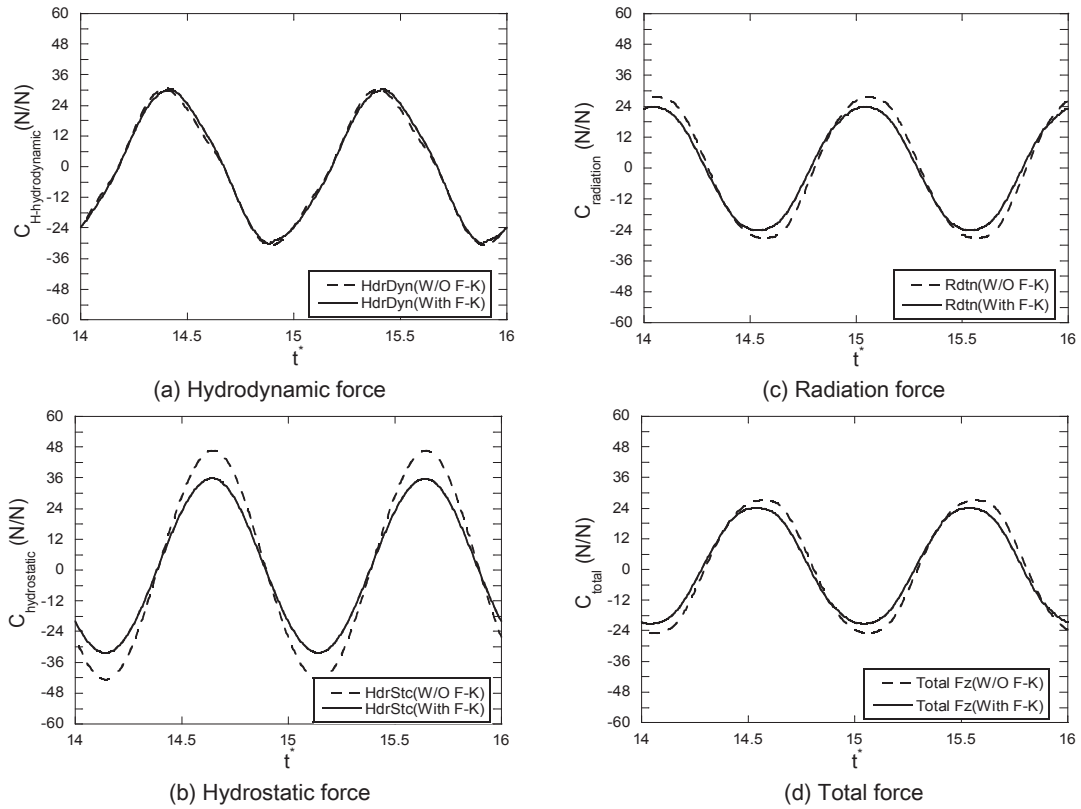

Fig. 15. Time series of (a) hydrodynamic force coefficient, (b) hydrostatic force coefficient, (c) radiation force coefficient and (d) total force coefficient in a regular wave with wave period of 2.6s.

respectively. The wave period corresponding to full scale is also shown in the figure. It is found that the surge RAO increases linearly with increasing wave period since the conducted wave period is far away from the surge natural period of floating system. In addition, dynamic motions are improved in the whole wave range when the axial F-K forces on slender members are considered, especially in the heave and pitch directions as shown in Fig. 13 (b) and (c). Phase differences shown in Fig. 13 between the incident wave and dynamic motion are improved as well. An accurate prediction of phase difference is of great importance in the evaluation of dynamic motions of FOWT since the hydrodynamic force is not only dependent on the incident wave but is also associated with the motion of platform itself.

To explain the effect of axial F-K force on the dynamic motion of the platform in regular waves, one case with wave period of 2.6s is discussed. Fig. 14 shows the measured and predicted time series of normalized surge, heave and pitch motions using the two different models as shown in Fig. 12. The good agreement between the measured and simulated incident wave elevation shown in Fig. 14(a) indicates that linear wave theory is suitable to simulate the incident wave generated in this water tank test. It is expected that the surge motion between those two sets of simulation is almost the same as shown in Fig. 14(b) since the contribution of the axial F-K force on the horizontal force component is negligible. The inclusion of this axial F-K force makes a difference in the total vertical hydrodynamic force. It is found that the heave motions shown in Fig. 14(c) deviate from the measured heave motions when the axial F-K forces are neglected, while the predicted heave motions are improved significantly after considering the axial F-K forces on slender members. The predicted pitch motion shown in Fig. 14(d) is also improved because the axial F-K force brings a change in the moment around the y-axis. Therefore, the axial F-K force contributes to the force component in the heave direction and improves heave and pitch motions significantly.

Vertical components of the external force expressed in Eq. (20) are extracted to clarify the effect of the axial F-K force on the dynamic response of FOWT. The radiation force is isolated from the total hydrodynamic force in Eq. (20). The total hydrodynamic force denotes the sum of F-K force, diffraction force and drag force. The radiation force corresponds to the effect of the motion of the platform. The hydrostatic force as expressed in Eq. (22) is also extracted since it is critical in the evaluation of the heave motion of the platform. The distributed forces on all submerged elements are summed up, and the total force is used for comparison.

The force components used for discussion are expressed in non-dimensional form as follows:

$$C_{hydrodynamic} = \frac{F_{hydrodynamic}}{1/2\rho_w(\omega H/2)^2 A} \tag{63}$$

$$C_{hydrostatic} = \frac{F_{hydrostatic}}{1/2\rho_w(\omega H/2)^2 A} \tag{64}$$

$$C_{radiation} = \frac{F_{radiation}}{1/2\rho_w(\omega H/2)^2 A} \tag{65}$$

$$C_{total} = \frac{F_{total}}{1/2\rho_w(\omega H/2)^2 A} \tag{66}$$

where $C_{hydrodynamic}$, $C_{hydrostatic}$, $C_{radiation}$, and C_{total} refer to the non-

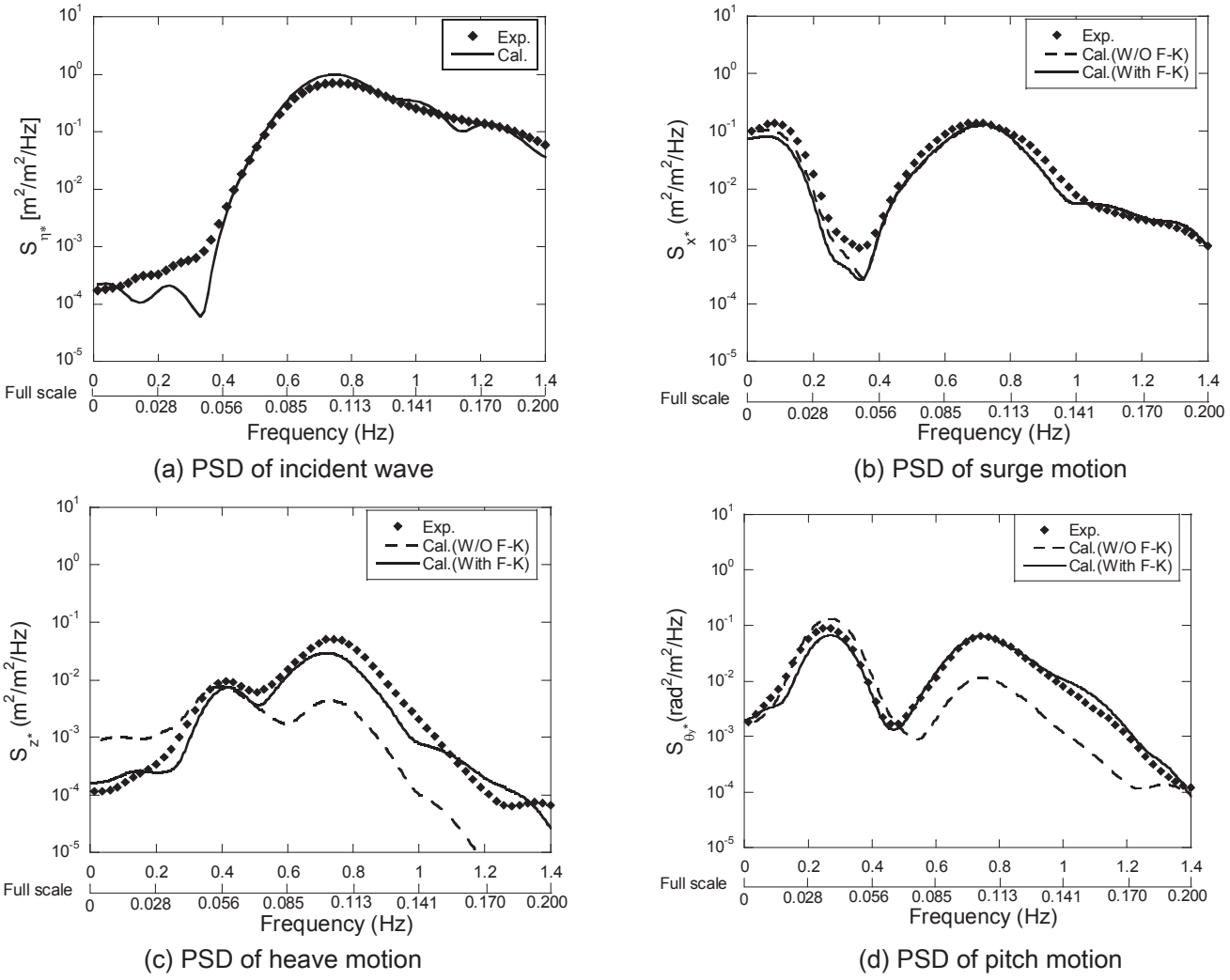

Fig. 16. Power spectrum density of (a) incident wave and dynamic response of (b) surge motion, (c) heave motion, and (d) pitch motion in an irregular wave (case 4).

dimensional total hydrodynamic force, hydrostatic force, radiation force, and total force coefficients, respectively; $F_{hydrodynamic}$, $F_{hydrostatic}$, $F_{radiation}$, and F_{total} represent the total hydrodynamic force, hydrostatic force, radiation force, and total force acting on the platform, respectively; A is the projected area of the three heave plates on the XY plane (0.185 m^2).

Fig. 15 shows the time series of vertical force components in the case shown in Fig. 14. It is found that the magnitude of hydrodynamic, hydrostatic and radiation forces are comparable. The time series of the hydrodynamic force shown in Fig. 15(a) is almost perfectly out of phase with the wave elevation. This is because the diffraction force is dominant, while the nonlinear drag force is negligible. The hydrostatic force shown in Fig. 15(b) is proportional to the difference between wave elevation and displacement of platform as expressed in Eq. (22) and Eq. (23) and it follows the out of phase heave motion of platform. The radiation force is found to be in-phase with the heave motion of platform as indicated by Eq. (20).

The effect of the axial F-K force on the resulting dynamic response of FOWT is explained here. Since the axial F-K force slightly changes the hydrodynamic force as shown in Fig. 15 (a), this leads to a slight difference in the heave motion of platform as shown in Fig. 14(c). As a result, the amplitudes of radiation force and the hydrostatic force decrease since they are directly associated with the heave motion of platform. Consequently, the total force shown in Fig. 15(d) decreases and mitigates the heave response of platform. It is important that hydrostatic and radiation forces amplify the effect of axial F-K force through the heave motion even though the axial F-K force contributes only a small fraction of the total force.

The dynamic response of FOWT in an irregular wave is simulated to investigate the performance of the proposed hydrodynamic model in a much wider range of wave frequency. Fig. 16(a) depicts the power spectrum density (PSD) of generated incident wave according to JONSWAP spectrum as described in Eq. (30). The good agreement between simulated and measured PSD of incident wave indicates that linear superposition of Airy wave is suitable for simulating the irregular wave generated in this water tank test. Fig. 16(b), (c), (d) show the measured and predicted PSD of dynamic responses in the surge, heave and pitch directions respectively. As shown in Fig. 16(b), there is no large difference in the PSD of surge motion of the platform between the two simulations with and without the axial F-K forces, which is consistent with the conclusion obtained in regular waves. In Fig. 16(c), the first peak of PSD of heave motion of the platform located at 0.42 Hz corresponds to the natural frequency of heave mode, where the resonant response is excited by low wave frequency components in the irregular wave. The second peak located at 0.75 Hz corresponds to the peak wave

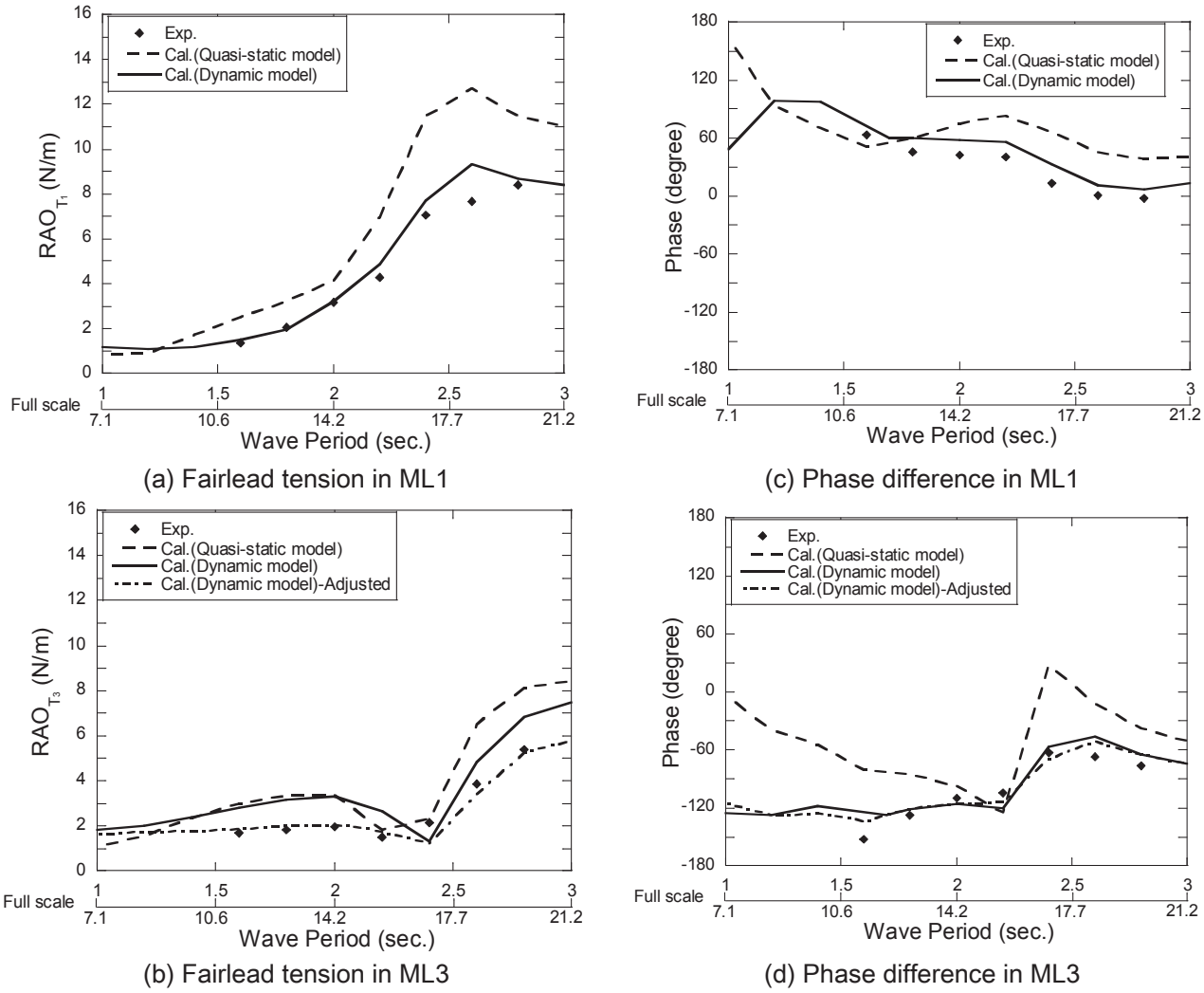

Fig. 17. Measured and predicted fairlead tension RAO and phase difference by quasi-static model and dynamic model in regular waves (case 3).

period of incident irregular wave. It is found that the wave-induced motion is improved significantly after the axial F-K forces on slender members are taken into account, especially in the wave frequency range of 0.5 Hz–1.0 Hz. This conclusion is consistent with the results shown in Fig. 13(b), in which heave RAO is improved in those short wave periods. It is also found that the PSD

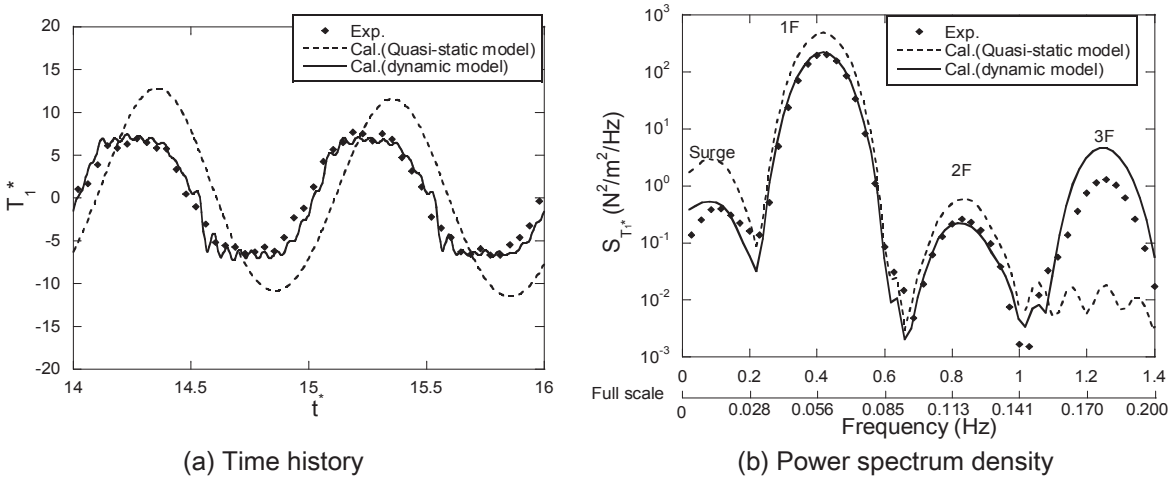

Fig. 18. Measured and predicted (a) time history and (b) power spectrum density of normalized fairlead tension in the mooring line 1 in a regular wave with wave period of 2.4s.

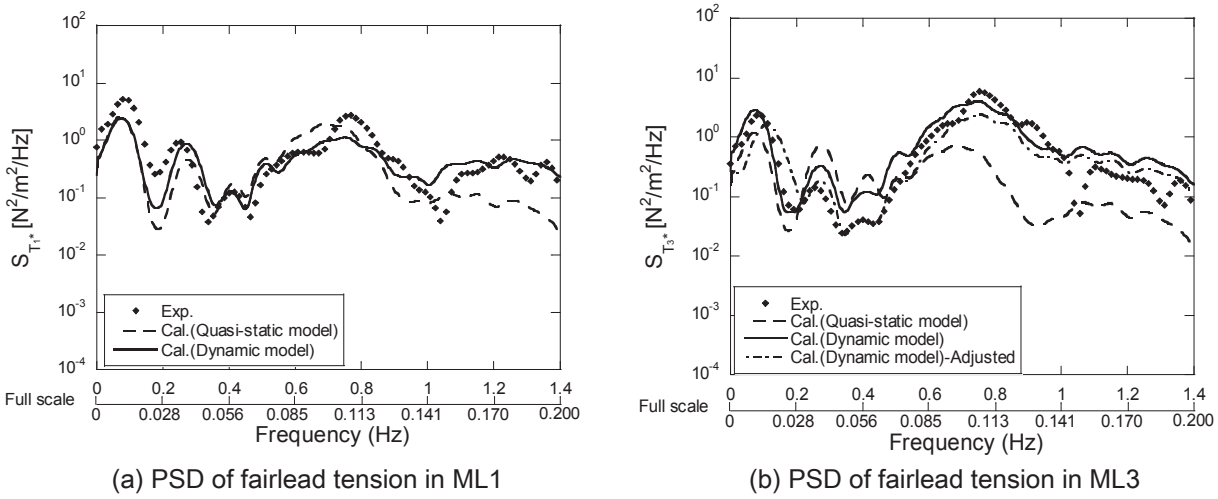

Fig. 19. Measured and predicted power spectrum density of normalized fairlead tension in an irregular wave (case 4).

of pitch motion of the platform is improved remarkably after considering the axial F-K forces on the slender members as shown in Fig. 16(d). Consequently, the proposed hydrodynamic model shows a good performance in both background and resonant responses across the whole wave frequency range.

4.4. Effect of dynamic behavior of mooring system

The impact of hydrodynamic behavior of the mooring line on fairlead tension prediction is clarified in this section. First, the mooring tension RAO in regular waves predicted by quasi-static model and dynamic models is presented. The performance of the two distinct models is then investigated by a regular wave with a period of 2.4 s. Mooring tension RAO is defined as:

$$RAO_{T_i} = \frac{A_{T_i}}{H/2} \tag{67}$$

where A_{T_i} refers to the amplitude of fairlead tension in each mooring line (i.e., ML1, ML2 and ML3 as shown in Fig. 5).

In the following discussion, the time series of fairlead tension is normalized as:

$$T_i^*(t^*) = \frac{T_i(t^*)}{H/2}; \quad t^* = \frac{t}{T} \tag{68}$$

where T_i^* refers to the normalized fairlead tension in ML1, ML2 and ML3; t^* is the non-dimensional time; T is the wave period of incident regular wave.

Fig. 17 shows the measured and predicted fairlead tension RAO and phase difference in the mooring lines expressed by ML1 and ML3. Phase difference refers to the phase between fairlead tension and incident regular wave. It is found that the quasi-static model apparently overestimates the fairlead tension RAO in all wave periods for ML1 and ML3, while the dynamic model provides a better prediction. In addition, accuracy of predicted phase differences by means of the dynamic model is improved as well. This is primarily due to the consideration of nonlinear drag force in the dynamic model, which shifts the phase of fairlead tension. The fairlead tension in ML3 is overestimated by dynamic model, which is due to the effect of the attached cable in the experiment, and it is improved by considering this effect as shown in Table 9.

In fact, an accurate prediction of the platform motion is critical for evaluation of fairlead tension since the mooring system is fully coupled with the dynamic response of platform. Favorable agreement between predicted and measured motion as shown in Fig. 13 is a solid foundation for satisfactory tension prediction by the dynamic model.

In the study by Hall et al. [16], the poor fairlead tension prediction by the dynamic model is primarily ascribed to the poor heave motion prediction.

The measured and predicted time series and PSD of fairlead tension in mooring line 1 by the quasi-static and dynamic models are shown in Fig. 18 for the case with a wave period of 2.4s. The initial fairlead tension in the mooring lines is removed and the fluctuation of fairlead tension is shown. As observed in Fig. 18(a), the quasi-static model overestimates the magnitude of fairlead tension in mooring line 1 by 51% and phase lag is observed between the measured and predicted fairlead tensions. In addition, harmonic components are observed in the measured fairlead tension whereas they are not reproduced by the quasi-static model. From the PSD shown in Fig. 18(b), harmonic components are observed from the measurement across the whole frequency domain. Among these peaks, the first one (0.09 Hz) corresponds to the natural frequency of the surge motion of platform and the second one (1F = 0.42 Hz) is excited by the motion owing to the first-order hydrodynamic loads on the platform and by the resonance of the heave motion of platform (0.42 Hz). This is why the second peak shows a large value. The third and fourth peaks are associated with the motion component caused by the nonlinear drag force acting on the platform and mooring lines, respectively; their frequency are two and three times as large as the frequency of the second peak. The quasi-static model could predict the components of the first three peaks, but, it fails to yield the higher harmonic components, such as 3F as shown in Fig. 18(b). In contrast to the quasi-static model, the dynamic model successfully predicts all harmonic components. In addition, the peaks predicted by the dynamic model match well with those observed from the measurement, while the first three peaks by the quasi-static model are overestimated. As a result, the influence of the dynamic behavior of the mooring line is significant in the evaluation of fairlead tension amplitude, and the drag coefficient for the chain is a key parameter in dynamic analysis of mooring system.

Finally, the PSDs of fairlead tensions in an irregular wave (case4 in Table 4) are presented in Fig. 19. The predicted PSDs of fairlead tensions show a favorable agreement with those measured in the water tank test when hydrodynamic force on mooring segments is taken into consideration by the dynamic model. The peaks

corresponding to the surge natural frequency are observed in ML1 and ML3. Since the pitch motion of platform leads to the displacement of mooring lines in the surge direction, the peaks with respect to the pitch natural frequency are also observed in the two mooring lines as well. The predicted fairlead tension for ML1 in the range of 0–0.2 Hz is slightly underestimated since the surge motion is underestimated in this range as shown in Fig. 16(b) resulting from the underestimation of the incident wave height shown in Fig. 16(a). The predicted fairlead tension for ML3 matches the measurement well in this frequency range, which may be due to overestimation of the fairlead tension by these two models. Overestimation of predicted fairlead tension for ML3 is also observed in the range of 0.2–0.7 Hz owing to the same reason as shown in Fig. 17(b), and it is improved when the additional force is applied on the tower base to simulate the effect of the attached cable. The predicted fairlead tension for ML1 in this range is improved by the dynamic model the same as those shown in Fig. 17(a). The predicted fairlead tensions for the two mooring lines by the dynamic model show a favorable agreement with the measurements in the range of 1.0–1.4 Hz, but those by the quasi-static model are underestimated as mentioned in Fig. 18(b), because the higher-order harmonic components are significantly underestimated by the quasi-static model in this frequency range.

5. Conclusions

A fully coupled nonlinear simulation tool is developed with the augmented Morison's equation, and correction factors for hydrodynamic coefficients are proposed. The predicted dynamic responses of FOWT are validated by the water tank tests. The conclusions are obtained as follows:

- The correction factors for added mass and drag coefficients used in the augmented Morison's equation are proposed to account for the effects of frequency dependent hydrodynamic coefficients and to provide consistent distributed hydrodynamic coefficients. The global matrices of hydrodynamic coefficients calculated by the proposed models show good agreement with those obtained from the forced oscillation tests.
- The effects of frequency dependent hydrodynamic coefficients and axial Froude-Krylov forces on slender members are clarified by the free decay tests and water tank tests with regular and irregular waves. The predicted dynamic motions of floating offshore wind turbine with the proposed hydrodynamic coefficients show good agreement with those obtained from the water tank tests, while the conventional Morison's equation underestimates the heave and pitch motions in the high frequency region and overestimates them in the low frequency region.
- The dynamic model successfully simulated all the harmonic components of fairlead tension measured by the water tank tests, but the quasi-static model only reproduced the first three peaks caused by the motions of the floater. The predicted amplitude of the fairlead tension in mooring line 1 by the quasi-static model is overestimated by 51%, while the dynamic model shows good agreement with the water tank test.

Acknowledgement

This research is carried out as a part of the Fukushima floating offshore wind farm demonstration project funded by the Ministry of Economy, Trade and Industry. The authors wish to express their deepest gratitude to the concerned parties for their assistance during this study.

References

[1] M.N. Schwartz, D. Heimiller, S. Haymes, W. Musial, Assessment of Offshore Wind Energy Resources for the United States, National Renewable Energy Laboratory, 2010.
[2] A.-K. Govindji, R. James, A. Carvallo, Appraisal of the Offshore Wind Industry in Japan, CARBON TRUST, 2014.
[3] GWEC : http://gwec.net/global-figures/graphs/.
[4] Hywind Demo: http://innovate.statoil.com/challenges/hywind/Pages/default.aspx.
[5] WindFloat:http://windfloatpacific.com/.
[6] GOTO FOWT:http://goto-fowt.go.jp/english/.
[7] Fukushima FORWARD: http://www.fukushima-forward.jp/english/index.html.
[8] J. Morison, J. Johnson, S. Schaaf, The force exerted by surface waves on piles, J. Petrol. Technol. 2 (05) (1950) 149–154.
[9] A. Robertson, J. Jonkman, F. Vorpahl, W. Popko, J. Qvist, L. Frøyd, et al., Offshore code comparison collaboration continuation within IEA wind task 30: phase II results regarding a floating semisubmersible wind system, in: ASME, vol. 2014, 2014, pp. 1–15.
[10] L. Sethuraman, V. Venugopal, Hydrodynamic response of a stepped-spar floating wind turbine: numerical modelling and tank testing, Renew. Energy 52 (2013) 160–174.
[11] OrcaFlex. Version 9.4 a, Orcina Ltd, 2010.
[12] P. Phuc, T. Ishihara, A study on the dynamic response of a semi-submersible floating offshore wind turbine system Part 2: numerical simulation, in: ICWE12. Cairns, Australia, 2007.
[13] M.B. Waris, T. Ishihara, Dynamic response analysis of floating offshore wind turbine with different types of heave plates and mooring systems by using a fully nonlinear model, Coupled Syst. Mech. 1 (3) (2012) 247–268.
[14] J.M. Jonkman, Dynamics Modeling and Loads Analysis of an Offshore Floating wind Turbine, National Renewable Energy Labortory, 2007.
[15] J. Browning, J. Jonkman, A. Robertson, A. Goupee, Calibration and validation of a spar-type floating offshore wind turbine model using the FAST dynamic simulation tool, J. Phys. Conf. 555 (2014) 012015.
[16] M. Hall, A. Goupee, Validation of a lumped-mass mooring line model with DeepCwind semisubmersible model test data, Ocean Eng. 104 (2015) 590–603.
[17] F. Huijs, E.-J. de Ridder, F. Savenije, Comparison of model tests and coupled simulations for a semi-submersible floating wind turbine, in: ASME 2014 33rd International Conference on Ocean, Offshore and Arctic Engineering, 2014.
[18] Bladed. Version 4.6, DNV GL, 2014.
[19] M. Hall, B. Buckham, C. Crawford, Evaluating the importance of mooring line model fidelity in floating offshore wind turbine simulations, Wind Energy 17 (12) (2014) 1835–1853.
[20] A.M. Viselli, A.J. Goupee, H.J. Dagher, C.K. Allen, Design and model confirmation of the intermediate scale VolturnUS floating wind turbine subjected to its extreme design conditions offshore Maine, Wind Energy 19 (6) (2016) 1161–1177.
[21] D. Matha, O. Bischoff, U. Fechter, M. Kuhn, Non-linear multi-body mooring system model for floating offshore wind turbines, in: EWEA Offshore 2011. Amstgerdam, Netherlands, 2011.
[22] M. Masciola, A. Robertson, J. Jonkman, A. Coulling, A. Goupee, Assessment of the importance of mooring dynamics on the global response of the deepcwind floating semisubmersible offshore wind turbine, in: The Twenty-third International Offshore and Polar Engineering Conference, 2013.
[23] AQWA. Version 15.0, ANSYS. Inc., 2013.
[24] T. Sarpkaya, Wave Forces on Offshore Structures, Cambridge University Press, 2010.
[25] S. Zhang, T. Ishihara, Predication of dynamic response of semi-submersible floating offshore wind turbine using Morison based theory, in: EWEA, 2015, pp. 17–21. Paris.
[26] A. Robertson, J. Jonkman, M. Masciola, H. Song, A. Goupee, A. Coulling, C. Luan, Definition of the Semisubmersible Floating System for Phase II of OC4. Offshore Code Comparison Collaboration Continuation (OC4) for IEA Task 30, 2012.
[27] H. Haslum, O. Faltinsen, Alternative shape of spar platforms for use in hostile areas, in: Offshore Technology Conference. Houston, Texas, 1999.
[28] L. Tao, S. Cai, Heave motion suppression of a Spar with a heave plate, Ocean Eng. 31 (5) (2004) 669–692.
[29] J.M. Jonkman, Dynamics of offshore floating wind turbines—model development and verification, Wind Energy 12 (5) (2009) 459–492.
[30] S. Ju, J. Stone, R. Rowlands, A new symmetric contact element stiffness matrix for frictional contact problems, Comput. Struct. 54 (2) (1995) 289–301.
[31] A. Couch, J. Conte, Field verification of linear and nonlinear hybrid wave models for offshore tower response prediction, J. Offshore Mech. Arctic Eng. 119 (3) (1997) 158–165.
[32] A. Kaveh, Computational Structural Analysis and Finite Element Methods, Springer, 2014.
[33] M.B. Waris, Fully Nonlinear Finite Element Model for Dynamic Response Analysis of Floating Offshore Wind Turbine System, PhD thesis, The University of Tokyo, 2010.
[34] P. Sachs, Wind Forces in Engineering, Elsevier, 2013.
[35] C.E. Brennen, A Review of Added Mass and Fluid Inertial Forces, Sierra Madre,

California, 1982.
[36] S. Zhang, T. Ishihara, Numerical study of hydrodynamic coefficients of multiple heave plates by large eddy simulations with volume of fluid method, Ocean Energy 163 (2018) 583–598.
[37] K. Shimada, T. Ishihara, Application of a modified k–ε model to the prediction of aerodynamic characteristics of rectangular cross-section cylinders, J. Fluid Struct. 16 (4) (2002) 465–485.
[38] DNV. recommended Practice DNV-rp-c205. Environmental Conditions and Environmental Loads, 2010.
[39] J. Li, S. Liu, M. Zhao, B. Teng, Experimental investigation of the hydrodynamic characteristics of heave plates using forced oscillation, Ocean Eng. 66 (2013) 82–91.
[40] C. Lopez-Pavon, A. Souto-Iglesias, Hydrodynamic coefficients and pressure loads on heave plates for semi-submersible floating offshore wind turbines: a comparative analysis using large scale models, Renew. Energy 81 (2015) 864–881.
[41] T. Ishihara, K. Kagaya, Y. Kikuchi, Dynamic analysis of floating offshore wind turbine system considering combined hydrodynamic loadings, in: EWEA Offshore 2013. Messe Frankfurt, Germany, 2013.